

1 **Entrainment and Dynamics of Ocean-derived Impurities within Europa's Ice**
2 **Shell**

3 **J. J. Buffo^{1,2}, B. E. Schmidt¹, C. Huber³, and C. C. Walker⁴**

4 ¹Georgia Institute of Technology ²Dartmouth College ³Brown University ⁴Woods Hole
5 Oceanographic Institution

6 Corresponding author: Jacob Buffo (jacob.j.buffo@dartmouth.edu)

7 **Key Points:**

- 8 • Planetary ices contain a chemical fingerprint inherited from the thermochemical properties
9 and dynamics of the parent liquid reservoir
- 10 • The refreezing of basal fractures and perched lenses in Europa's ice shell produces regions
11 of high chemical gradation and concentration
- 12 • Europa's ice shell is predicted to have a bulk salinity between 1.053-14.72 ppt, depending
13 on the ocean composition

14 Abstract

15 Compositional heterogeneities within Europa's ice shell likely impact the dynamics and
16 habitability of the ice and subsurface ocean, but the total inventory and distribution of impurities
17 within the shell is unknown. In sea ice on Earth, the thermochemical environment at the ice-ocean
18 interface governs impurity entrainment into the ice. Here, we simulate Europa's ice-ocean interface
19 and bound the impurity load (1.053-14.72 g/kg (parts per thousand weight percent, or ppt) bulk ice
20 shell salinity) and bulk salinity profile of the ice shell. We derive constitutive equations that predict
21 ice composition as a function of the ice shell thermal gradient and ocean composition. We show
22 that evolving solidification rates of the ocean and hydrologic features within the shell produce
23 compositional variations (ice bulk salinities of 5-50% of the ocean salinity) that can affect the
24 material properties of the ice. As the shell thickens, less salt is entrained at the ice-ocean interface,
25 which implies Europa's ice shell is compositionally homogeneous below ~ 1 km. Conversely, the
26 solidification of water filled fractures or lenses introduces substantial compositional variations
27 within the ice shell, creating gradients in mechanical and thermal properties within the ice shell
28 that could help initiate and sustain geological activity. Our results suggest that ocean materials
29 entrained within Europa's ice shell affect the formation of geologic terrain and that these structures
30 could be confirmed by planned spacecraft observations.

31 Plain Language Summary

32 Europa, the second innermost moon of Jupiter, likely houses an interior ocean that could provide
33 a habitat for life. This ocean resides beneath a 10-30 km thick ice shell which could act as a
34 barrier or conveyor for ocean-surface material transport that could render the ocean chemistry
35 either hospitable or unfavorable for life. Additionally, material impurities in the ice shell will alter
36 its physical properties and thus affect the global dynamics of the moon's icy exterior. That said,
37 few of the interior properties of the ice shell or ocean have been directly measured. On Earth, the
38 composition of ocean-derived ice is governed by the chemistry of the parent liquid and the rate at
39 which it forms. Here we extend models of sea ice to accommodate the Europa ice-ocean
40 environment and produce physically realistic predictions of Europa's ice shell composition and
41 the evolution of water bodies (fractures and lenses) within the shell. Our results show that the
42 thermal gradient of the ice and the liquid composition affect the formation and evolution of
43 geologic features in ways that could be detectable by future spacecraft (e.g. by ice penetrating
44 radar measurements made by Europa Clipper).

46 1. Introduction

47 Europa's ocean was the first detected beyond Earth [*Khurana et al.*, 1998; *Kivelson et al.*,
48 2000]. Studies [*Cassen et al.*, 1979; *Pappalardo et al.*, 1999; *Ross and Schubert*, 1987; *Squyres et*
49 *al.*, 1983] indicate that Europa's internal structure hosts a thick global ocean bounded by a silicate
50 mantle below and a water ice shell above. These findings have fueled interest in the moon's interior
51 dynamics, which may facilitate environments suitable for life (e.g. [*Chyba and Phillips*, 2001;
52 *NRC*, 2011; *Des Marais et al.*, 2008; *Reynolds et al.*, 1983; *Russell et al.*, 2017]). Europa's ice
53 shell plays a crucial role in the moon's dynamics and evolution, as both a barrier and conveyor
54 between the ocean and surface. With most of the data available for Europa derived from remote
55 sensing techniques, the ice shell is a primary medium through which the properties of the ocean
56 and interior can be understood, as the ice expresses how the body has evolved through its geology
57 and composition. However, at present many of the ice shell's properties are not well constrained,
58 including ice thickness, ice chemistry, and the distribution of shallow water [*Billings and*

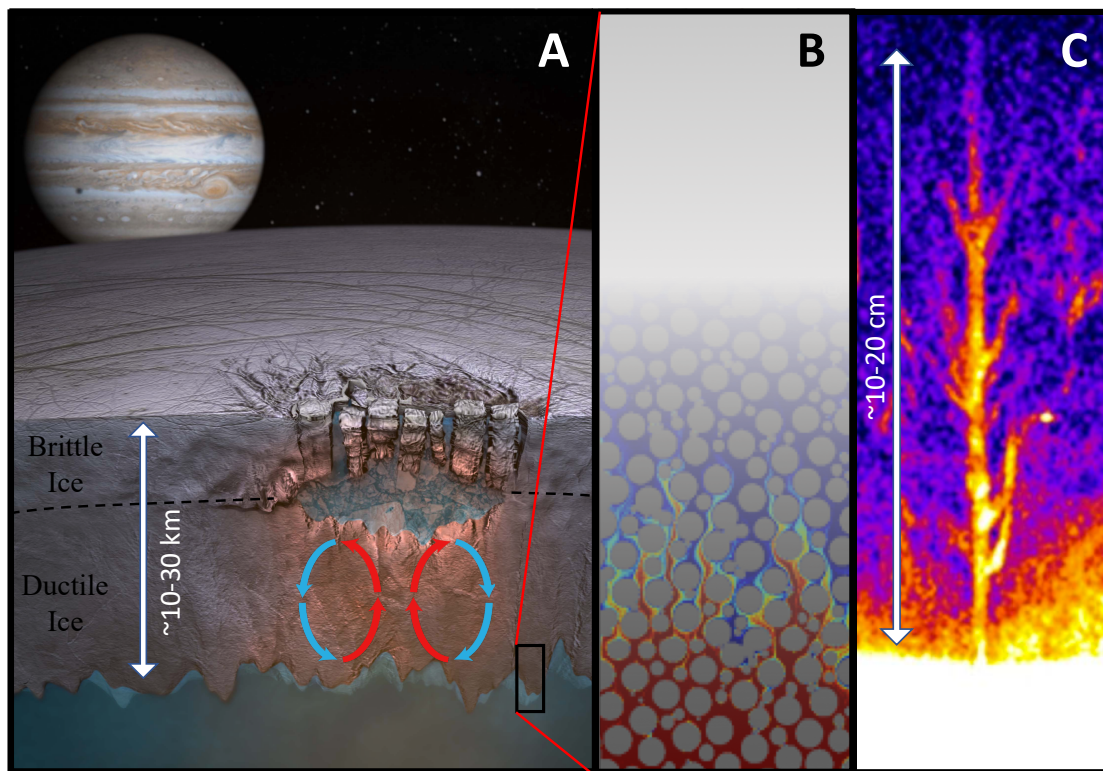
59 *Kattenhorn, 2005; Schmidt et al., 2011; Walker and Schmidt, 2015; Zolotov and Shock, 2001*.
60 Constraining characteristics of the European environment, locating potentially habitable niches,
61 understanding the transport processes supporting them, and investigating their connectivity are
62 planned objectives of the Europa Clipper mission [*Phillips and Pappalardo, 2014*]. As such,
63 quantifying the physical, thermal, chemical, and mechanical properties of the ice shell is
64 imperative to understanding Europa's geophysical and material transport processes that control its
65 habitability.

66 Heterogeneities in the ice shell have been linked to a number of proposed dynamic
67 processes: solid state convection in the lower ice shell [*Han and Showman, 2005; Howell and*
68 *Pappalardo, 2018; McKinnon, 1999*], subduction or subsumption of surface material [*Johnson et*
69 *al., 2017a; Kattenhorn, 2018; Kattenhorn and Prockter, 2014*], eutectic melting that may lead to
70 the formation of chaos and lenticulae [*Manga and Michaut, 2017; Michaut and Manga, 2014;*
71 *Schmidt et al., 2011*], formation and sustenance of water bodies within the shell [*Kargel et al.,*
72 *2000; Zolotov and Kargel, 2009*]. Yet the process by and rate at which impurities are entrained
73 within the ice remain poorly constrained, and while current models implement a range of potential
74 impurity loads to test model sensitivity to variations in ice composition [*Han and Showman, 2005;*
75 *Johnson et al., 2017b; Pappalardo and Barr, 2004*] they do not predict ice composition directly.
76 Furthermore, observations reveal that young, active terrain is richer in non-ice material than the
77 average ice [*McCord et al., 2002*] (Supplementary Figure S1), suggesting recent interaction with
78 subsurface water reservoirs enriched with salts [*Manga and Michaut, 2017; Michaut and Manga,*
79 *2014; Schmidt et al., 2011*], the effusion of ocean materials through fractures [*Fagents, 2003*], or
80 melt through of a thin ice shell [*Greenberg et al., 1999*].

81 When ice forms in an aqueous environment, it preserves a thermochemical record of the
82 water from which it formed [*Feltham et al., 2006; Gross et al., 1977; Hunke et al., 2011; Turner*
83 *and Hunke, 2015; Untersteiner, 1968*]. For Europa, the ice shell grew from the freezing of, and is
84 thus a window into, the ocean [*Bhatia and Sahijpal, 2017; Zolotov and Kargel, 2009; Zolotov and*
85 *Shock, 2001*]. With a geologically young surface ($<10^8$ yr [*Carr et al., 1998*]) suggesting active
86 ice shell overturn, dynamic regions of Europa's surface (e.g. bands and chaos) may harbor 'fossil
87 ocean material' entrained in the ice shell as recently as one million years ago [*Howell and*
88 *Pappalardo, 2018*]. This could provide an accessible sample of the contemporary ocean, as it is
89 highly likely that Europa's ice, much like sea ice and marine ice on Earth, contains pockets and
90 channels filled with brine, salts, gasses, and other impurities derived from the dynamics of freezing
91 at the ice-ocean interface [*Eicken, 2003; Pappalardo and Barr, 2004; Zolotov and Kargel, 2009;*
92 *Zotikov et al., 1980*] (See Figure 1). On Earth, sea ice captures such a record of the thermochemical
93 processes in the upper ocean during its formation. As the ocean solidifies, dissolved solutes are
94 rejected as crystalline ice forms and a porous water-ice matrix filled with hypersaline interstitial
95 fluid is produced [*Buffo et al., 2018; Feltham et al., 2006; Hunke et al., 2011; Turner and Hunke,*
96 *2015; Untersteiner, 1968; Weeks and Lofgren, 1967*]. This process produces a compositionally-
97 driven gravitational instability in the newly formed porous ice layer that results in buoyancy-driven
98 convection of the denser pore fluid into the underlying liquid reservoir. Referred to as gravity
99 drainage, this process has been observed to be the primary method of desalination during sea ice
100 formation and has been successfully incorporated into a number of numerical models [*Buffo et al.,*
101 *2018; Griewank and Notz, 2013; Huppert and Worster, 1985; Turner and Hunke, 2015; Wells et*
102 *al., 2011; Worster, 1991*].

103 Quantifying the relationship between Europa's ice composition and interfacial
104 thermochemistry at the time of formation would provide a technique for linking observed ice

105 properties to characteristics of its parent liquid water reservoir (a ‘frozen fingerprint’ of the source
 106 water) and forecasting the properties of ice produced under diverse thermal and chemical
 107 conditions – informing the synthesis of future mission data and geodynamic models. Impurities
 108 and structural heterogeneities within ice alter its thermal, physicochemical, and dielectric
 109 properties [Feltham *et al.*, 2006; Hunke *et al.*, 2011; Weeks and Ackley, 1986]. Thus, beyond the
 110 ice shell’s chemistry, the dynamics of impurity entrainment will affect the potentially appreciable,
 111 and ongoing, hydrological activity within Europa’s ice shell in the form of perched water lenses,
 112 fractures, dikes, and sills (e.g. [Manga and Michaut, 2017; Michaut and Manga, 2014; Schmidt *et al.*,
 113 2011; Walker and Schmidt, 2015]). Moreover, interpretation of measurements taken by Europa
 114 Clipper’s ice penetrating radar, REASON, depend critically on ice composition and dielectric
 115 properties [Blankenship *et al.*, 2009; Kalousova *et al.*, 2017; Weeks and Ackley, 1986]. If the ice
 116 shell is impurity rich it has the potential to reflect and attenuate radar signals, which can be used
 117 to investigate the ice shell’s interior structure but may also prevent observation of the ice-ocean
 118 interface [Kalousova *et al.*, 2017].
 119



120
 121 **Figure 1 – The Europa ice-ocean system.** **A)** A brittle ice lithosphere overlies a ductile ice mantle (dashed line) in
 122 contact with a subsurface ocean. A diapir generated perched water lens is an example of a putative hydrological feature
 123 within the ice shell that may facilitate the surface expression of recently entrained ocean material. **B)** Akin to terrestrial
 124 environments, the ice-ocean interface of Europa will likely be characterized by a two-phase ice-brine system, allowing
 125 solutes and other ocean material to be trapped within pore spaces (blue to red color scheme qualitatively depicts the
 126 thermal profile that results from local thermodynamic equilibrium in the mushy layer as well as cold, saline
 127 downwellings which lead to the formation of brine channels). **C)** Brine channels in terrestrial sea ice. The warm
 128 (yellow) to cool (blue/black) coloring corresponds to liquid fraction (pure fluid at the base of the image, low liquid
 129 fraction ice at the top of the image). (Image Credit: A – Adapted from Britney Schmidt/Dead Pixel FX, UT Austin. B
 130 – Adapted from [Rolle and Le Borgne, 2019] C – Adapted from [Worster and Rees Jones, 2015])
 131

132 To constrain the impurity load within Europa’s ice shell and investigate the possible
 133 dynamics associated with the presence of salt in the ice shell, we constructed a one-dimensional
 134 reactive transport model adapted from the sea ice model of *Buffo et al.* [2018] for the Europa
 135 environment and derive constitutive equations that describe the dependence of impurity content in
 136 ice on the thermodynamic conditions in which it forms. We performed simulations of the formation
 137 and evolution of Europa’s ice shell, validated against empirical observations of sea ice and marine
 138 ice growth rates and composition. The simulations include fluid and solute transport and the
 139 associated impurity entrainment that occurs at ice-ocean/brine interfaces. The model actively
 140 tracks the dynamic ice-ocean/brine interface as it propagates and catalogs the composition of the
 141 ice when it becomes impermeable and traps solutes within the ice. Since the ice composition
 142 derives from the initial ocean, we test an array of putative European ocean chemistries and thermal
 143 regimes and derive constitutive relationships between entrainment rates and the local thermal and
 144 chemical environment.

145 2. Methods

146 *2.1 Numerical Model*

147 The growth and evolution of the ice-ocean/brine interface is treated using an adapted
 148 version of the one-dimensional, two-phase, reactive transport model of sea ice described by *Buffo*
 149 *et al.* [2018]. Water/ice mass, energy, and salinity are conserved using a coupled set of equations
 150 that combines mushy layer theory and the enthalpy method. The governing equations are:
 151

$$152 \quad \bar{\rho}c \frac{\partial T}{\partial t} = \left(\bar{k} \frac{\partial^2 T}{\partial z^2} \right) - \rho_{\text{ice}} L \frac{\partial \phi}{\partial t} \quad (1)$$

$$153 \quad \phi \frac{\partial S_{\text{br}}}{\partial t} = \left(\bar{D} \frac{\partial^2 S_{\text{br}}}{\partial z^2} \right) - \frac{\rho_{\text{ice}}}{\rho_{\text{br}}} S_{\text{br}} \frac{\partial \phi}{\partial t} \quad (2)$$

$$154 \quad H = c_{\text{ice}} T + L\phi \quad (3)$$

$$155 \quad \phi = \begin{cases} 0 & H < H_s = c_{\text{ice}} T_m \\ (H - H_s)/L & \text{if } - H_s \leq H \leq H_s + L \\ 1 & H > H_s + L \end{cases} \quad (4)$$

156 where ρ is density, c is specific heat capacity, T is temperature, t is time, z is the vertical
 157 coordinate, k is heat conductivity, L is the latent heat of fusion for the water to ice phase
 158 transformation, ϕ is liquid fraction, S is salinity, D is salt diffusivity, H is enthalpy, H_s is the
 159 enthalpy of a discretization cell consisting of only solid ice, and T_m is melting/freezing
 160 temperature. Subscripts ‘ice’ and ‘br’ refer to characteristics of the ice and brine components of
 161 the two-phase mixture, respectively, and variables carrying an over bar are volumetrically
 162 averaged quantities (i.e. $\bar{y} = \phi y_{\text{br}} + (1 - \phi) y_{\text{ice}}$). Equations 1 and 2 ensure conservation of heat
 163 and mass, respectively, and equations 3 and 4, combined, make up the enthalpy method. All
 164 variables and values used throughout the text can be found in Table 1.

165 The desalination of forming ice is governed by brine expulsion and gravity drainage. Brine
 166 expulsion refers to the phase change driven flux of hypersaline brine within the porous ice matrix

172 into the underlying liquid reservoir. As a volume containing both ice and brine components
 173 continues to solidify, assuming incompressible flow, conservation of mass requires that brine must
 174 be expelled from the volume. This is due to the density difference between ice and water. Given
 175 the unidirectional solidification scenarios considered here, the brine will move downward into the
 176 ambient ocean/brine. Gravity drainage refers to the buoyancy-driven convective overturn of brine
 177 within the permeable multiphase layer. Both effects were considered by the model of Buffo et al.
 178 (2018); however, in line with previous research [*Griewank and Notz, 2013; Wells et al., 2011*],
 179 gravity drainage was shown to be the primary mode of desalination. As such, with minimal loss
 180 of accuracy, we forego simulating phase change driven Darcy flow (brine expulsion) in the porous
 181 ice and opt to use the one-dimensional gravity drainage parameterization of *Griewank and Notz*
 182 [2013] to represent fluid transport. This parameterization represents the process of gravity drainage
 183 through brine channels as a linear function of the local Rayleigh number, and is widely used for
 184 solving multiphase melting/solidification problems [*Griewank and Notz, 2013; Turner and Hunke,*
 185 *2015; Turner et al., 2013; Wells et al., 2011*]. Here, the mass of brine transported out of a
 186 discretized layer j (See Figure 2 for model schematic) is given as:

187

$$188 \quad br_j^\downarrow = \alpha(Ra_j - Ra_c)dz^3dt = \alpha \left(\frac{g\rho_{sw}\beta\Delta S_j\tilde{\Pi}h_j}{\kappa\mu} - Ra_c \right) dz^3dt \quad (5)$$

189

190 where α is a constant of proportionality, Ra_j is the Rayleigh number of the j^{th} layer, Ra_c is the
 191 critical Rayleigh number, dz and dt are the spatial and temporal discretization sizes, respectively,
 192 g is acceleration due to gravity, ρ_{sw} is the density of the ambient reservoir fluid (ocean/brine), β
 193 is a density coefficient describing the relationship between density and salinity, ΔS_j is the
 194 difference in salinity of the brine in the j^{th} layer and the ambient ocean, h_j is the height of the j^{th}
 195 layer above the basal surface of the ice, κ is the thermal diffusivity of seawater, μ is the kinematic
 196 viscosity of seawater, and $\tilde{\Pi}_j$ is the minimum permeability of any layer between the j^{th} layer and
 197 the basal ice surface. The permeability function given by *Griewank and Notz (2013) [Freitag,*
 198 *1999]* is utilized:

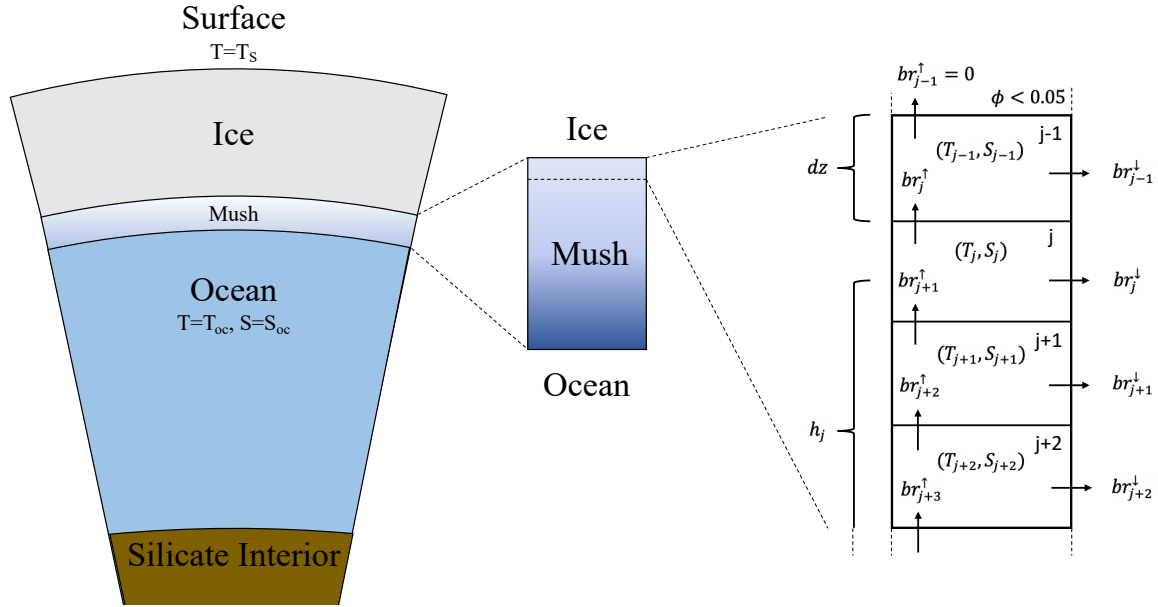
199

$$200 \quad \Pi(\phi) = 10^{-17}(10^3\phi)^{3.1} \quad (6)$$

201

202 and a critical porosity cutoff is implemented to prevent drainage from layers containing low liquid
 203 fractions (here $\phi < 0.05$ [*Golden et al., 2007*] results in a layer's fluid transport being shut off).
 204 Heat and salt are transported out of the model domain by this convective process and the equations
 205 of mushy layer theory (Eq. 1 & 2) are modified accordingly (receiving a new term, $br_j^\downarrow \partial T / \partial z$ and
 206 $br_j^\downarrow \partial S / \partial z$, respectively, on their right hand sides representing advective flux due to gravity
 207 drainage – See Eq. 16). Equations 1-4 are solved using an implicit finite difference method, a
 208 standard second order spatial discretization for the diffusion terms, and an upwind scheme for the
 209 advective terms to produce spatiotemporal profiles of temperature, salinity, and porosity at the ice-
 210 ocean interface.

211



212
 213 **Figure 2 – Advective fluxes and model discretization.** Implementing the one-dimensional gravity drainage
 214 parameterization of [Griewank and Notz, 2013] results in the transport dynamics shown here. Downwelling
 215 brine velocities (e.g. br_j^\downarrow) are taken to be a linear function of the local Rayleigh number (Ra_j of Eq. 5) and conservation of
 216 mass (replacement of downwelling brine by upwelling brine, e.g. br_{j+1}^\uparrow) guarantees that advective fluxes of continuum
 217 properties (T_j, S_j) are represented by $br_j^\downarrow \partial(T_j, S_j) / \partial z$, where z is positive downward.

218
 219 It is important to note that ‘salinity’, here, refers to a bulk property of the fluid
 220 representative of the ion species present (i.e. utilizing a singular molecular diffusivity value). In
 221 reality, individual ion species diffusivities vary and when combined with complex ion-ion
 222 interactions can lead to additional chemical processes (e.g. double diffusion, hydrate precipitation,
 223 fractionation) that may alter the composition of the forming ice and brine (e.g. [Vance et al.,
 224 2019]). Our approach provides a first order estimate of salt and impurity entrapment in planetary
 225 ices and creates the potential for follow-on research investigating the detailed thermochemistry of
 226 ices and brines in our solar system through the use of contemporary chemical modeling tools such
 227 as PHREEQC, the Gibbs SeaWater (GSW) Oceanographic Toolbox, and SeaFreeze [Journaux et
 228 al., 2020; McDougall and Barker, 2011; Neveu et al., 2017].

229 For this work, we update the model of Buffo et al. [2018] to include active interface
 230 tracking. Modeling the entire ice shell thickness and lifespan at the resolution needed to capture
 231 the reactive transport dynamics occurring near the ice-ocean/brine interface is computationally
 232 intractable. To overcome these difficulties, we modified our model [Buffo et al., 2018] such that it
 233 actively tracks only the permeable or ‘active’ region of the ice shell, determined by the critical
 234 porosity where fluid flow ceases (e.g. [Golden et al., 1998; Golden et al., 2007]). In the top-down
 235 solidification scenarios modeled, when the fluid fraction of a discretized layer drops below the
 236 critical porosity it is removed from the active domain and its properties are cataloged, along with
 237 all the cells above it, and an equal number of replacement layers are added to the bottom of the
 238 domain with ambient ocean/brine characteristics ($T_{oc}, S_{oc}, \rho_{sw}$). This enables the efficient
 239 simulation of much thicker regions of ice growth (10s-100s of meters vs. 10s-100s of centimeters)
 240 over much longer times (10s-1000s of years vs. 10s-100s days) by removing ‘dead’ cells which
 241 are no longer interacting with the underlying ocean. This is a novel addition to existing reactive

242 transport models of ocean-derived ices (e.g. [Cox and Weeks, 1988; Griewank and Notz, 2013;
 243 Turner et al., 2013]) and specifically resolves the difficulty of accurately simulating the
 244 physicochemical evolution of thick planetary ices.

245

Symbol	Definition	Value	Units
α	1D Advection Coefficient	1.56×10^{-1}	$\text{kg m}^{-3} \text{s}^{-1}$
β	Density (Salinity) Coefficient	5.836×10^{-4}	kg ppt^{-1}
$br^{\uparrow, \downarrow}$	Vertical Brine Transport	Calculated	kg
c_{br}	Brine Heat Capacity	3985	$\text{J kg}^{-1} \text{K}^{-1}$
c_{ice}	Ice Heat Capacity	2000	$\text{J kg}^{-1} \text{K}^{-1}$
D	Salt Diffusivity	Calculated	$\text{m}^2 \text{s}^{-1}$
g	Acceleration Due to Gravity	1.32/9.8	m s^{-2}
h	Distance to Interface	Calculated	m
H_{shell}	Ice Shell Thickness	Varies	m
H	Enthalpy	Calculated	J kg^{-1}
H_s	Enthalpy of Solid Cell	Calculated	J kg^{-1}
k_{br}	Brine Heat Conductivity	0.6	$\text{W m}^{-1} \text{K}^{-1}$
k_{ice}	Ice Heat Conductivity	2	$\text{W m}^{-1} \text{K}^{-1}$
κ	Thermal Diffusivity	Varies	$\text{m}^2 \text{s}^{-1}$
L, L_f	Latent Heat of Fusion	334,774	J kg^{-1}
λ	Coefficient Dependent on St	Calculated	-
μ	Kinematic Viscosity	1.88×10^{-3}	$\text{m}^2 \text{s}^{-1}$
ϕ	Liquid Fraction	Calculated	-
ϕ_c	Critical Porosity	0.05	-
Π	Permeability	Calculated	m^2
Ra	Rayleigh Number	Calculated	-
Ra_c	Critical Rayleigh Number	1.01×10^{-2}	-
ρ_{br}	Brine Density	Varies	kg m^{-3}
ρ_{ice}	Ice Density	917	kg m^{-3}
ρ_{sw}	Ocean/Reservoir Density	Varies	kg m^{-3}
S	Salinity	Calculated	ppt
S_{lim}	Minimum Salinity	Varies	ppt
S_{oc}	Ocean/Reservoir Salinity	Varies	ppt
S_{tot}	Bulk Salinity/Total Salt	Calculated	ppt
St	Stefan Number	Calculated	-
t	Time	-	s
T	Temperature	Calculated	K
T_0	Supercooled Temperature	Varies	K
T_1	Liquid Temperature	Varies	K
T_m	Melting/Freezing Temperature	Varies	K
T_{oc}	Ocean Temperature	Varies	K
T_s	Surface Temperature	100	K
v_m	Freezing Front Velocity	Calculated	m s^{-1}
x_m	Freezing Front Position	Calculated	m
z	Vertical Coordinate	-	m

246 **Table 1 – Variables.** All variables used in the text, along with their definition, values, and units.

247

248 2.2 The Stefan Problem: Deriving the Constitutive Equations

249 The interpolation of results used to derive the constitutive relationships between ice
 250 characteristics and the thermochemical environment hinges on the ability to fit the simulated data
 251 to a predefined function. The form of this function should be representative of the physical
 252 processes occurring within the simulation. As the equations governing the multiphase reactive
 253 transport model do not lend themselves to an analytical solution, it is logical to seek a simplified

254 system that does. To investigate the evolution of dissolved salt in an ice-ocean environment we
 255 make a number of simplifying assumptions and solve Equation 2 analytically.

256 The classic Stefan problem describes the dynamics and evolution of pure substance
 257 melting/solidification and is well documented in the literature [*Huber et al.*, 2008; *Michaut and*
 258 *Manga*, 2014; *Rubinštejn*, 2000]. The basic geometry of the problem can be seen in Supplementary
 259 Figure S2. The analytical solution of the thermal profile in the solid and the time dependent
 260 solidification front is [*Huber et al.*, 2008]:

261

$$262 \quad T(x, t) = T_0 - (T_0 - T_1) \frac{\operatorname{erf}\left(\frac{x}{2\sqrt{\kappa t}}\right)}{\operatorname{erf}(\lambda)} \quad (7)$$

263

$$264 \quad x_m(t) = 2\lambda\sqrt{\kappa t} \quad (8)$$

265

$$266 \quad \lambda \exp(\lambda^2) \operatorname{erf}(\lambda) = \frac{St}{\sqrt{\pi}} = \frac{c(T_0 - T_1)}{L_f \sqrt{\pi}} \quad (9)$$

267

268 where $T(x, t)$ is the temperature within the solid at position x and time t , T_0 is the temperature at
 269 the undercooled surface and is lower than the melting temperature of the solid, T_1 is the
 270 temperature of the liquid, κ is the thermal diffusivity of the solid, x_m is the position of the
 271 solidification front, λ is a coefficient depending on St , erf is the error function, St is the Stefan
 272 number defined as $St = c(T_0 - T_1)/L_f$, c is the specific heat of the solid, and L_f is the latent heat
 273 of fusion for the water-ice phase transition.

274 While the Stefan problem represents a simpler system than that of our reactive transport
 275 model, the underlying physics governing solidification are the same and similar behavior is to be
 276 expected. It has been suggested that the amount of impurities entrained in forming ice is related to
 277 the rate at which the ice forms [*Nakawo and Sinha*, 1984; *Weeks and Ackley*, 1986; *Zolotov and*
 278 *Kargel*, 2009]. Equations 7-9 can be utilized to investigate the relationships between the rate of
 279 ice formation and both the freezing front position and local thermal gradient. First, differentiating
 280 Equation 8 with respect to time gives:

281

$$282 \quad v_m(t) = \dot{x}_m(t) = \frac{\lambda\kappa}{\sqrt{\kappa t}} = \frac{2\lambda^2\kappa}{x_m(t)} \quad (10)$$

283

$$284 \quad \Rightarrow v_m(t) \propto \frac{1}{x_m(t)} \quad (11)$$

285

286 where $v_m(t)$ is the solidification front velocity, which is equivalent to the rate of ice formation.
 287 Thus, the rate of ice formation is inversely proportional to the position of the solidification front.
 288 Second, differentiating Equation 7 with respect to position gives:

289

$$290 \quad \frac{\partial T(x, t)}{\partial x} = -\frac{(T_0 - T_1)}{\operatorname{erf}(\lambda)} \frac{1}{\sqrt{\pi\kappa t}} \exp(-x^2/4\kappa t) \quad (12)$$

291

292 At the position of the solidification front, $x_m(t) = 2\lambda\sqrt{\kappa t}$, Equation 12 becomes:

293
294

$$295 \quad \frac{\partial T(x_m, t)}{\partial x} = -\frac{(T_0 - T_1)}{\text{erf}(\lambda)} \frac{1}{\sqrt{\pi\kappa t}} \exp(-\lambda^2) \quad (13)$$

296

297 From Equation 10 we see that $\sqrt{\kappa t} = \lambda\kappa/v_m(t)$. Substituting this result into Equation 13 gives:

298

$$299 \quad \frac{\partial T(x_m, t)}{\partial x} = -\frac{(T_0 - T_1)}{\text{erf}(\lambda)} \frac{1}{\sqrt{\pi}\lambda\kappa} \exp(-\lambda^2)v_m(t) \quad (14)$$

300

$$301 \quad \Rightarrow \frac{\partial T(x_m, t)}{\partial x} \propto v_m(t) \quad (15)$$

302

303 The rate of ice formation is directly proportional to the local thermal gradient at the solidification
304 front. The relationships derived in Equations 11 & 15 provide insight into the spatiotemporal
305 evolution of the Stefan problem and its dependence on the local thermal environment. These results
306 will be utilized below, where a modified Stefan problem (inclusion of a solute and fluid dynamics)
307 is described and an analytical solution is derived. This solution describes the spatial and temporal
308 distribution of the solute and provides the functional form of the constitutive equations used
309 throughout the text.

310 To investigate the evolution of dissolved salt in an ice-ocean environment we make a
311 number of simplifying assumptions and solve Equation 2 analytically. Assuming top-down
312 unidirectional solidification of a salty ocean (e.g. sea ice, European ocean solidification) the
313 evolution of salt in the system can be described by the equations of reactive transport (Equation 2
314 including the gravity drainage parameterization, with br subscripts dropped from S terms for
315 simplicity):

316

$$317 \quad \phi \frac{\partial S}{\partial t} = \left(\bar{D} \frac{\partial^2 S}{\partial z^2} \right) - \frac{\rho_{\text{ice}}}{\rho_{\text{br}}} S \frac{\partial \phi}{\partial t} + br_j^\downarrow \frac{\partial S}{\partial z} \quad (16)$$

318

319 where br_j^\downarrow is the brine velocity in the j th layer described by the one-dimensional gravity drainage
320 parameterization. Introducing a new coordinate, ξ , such that $\xi = z - z_m(t)$, places the origin at
321 the ice-ocean interface and constitutes a moving coordinate system. In this new coordinate system
322 Equation 16 can be written as:

323

$$324 \quad \phi \frac{\partial S}{\partial \xi} \frac{\partial \xi}{\partial t} = \bar{D} \left[\frac{\partial^2 S}{\partial \xi^2} \left(\frac{\partial \xi}{\partial z} \right)^2 + \frac{\partial S}{\partial \xi} \frac{\partial^2 \xi}{\partial z^2} \right] - \frac{\rho_{\text{ice}}}{\rho_{\text{br}}} S \frac{\partial \phi}{\partial \xi} \frac{\partial \xi}{\partial t} + br_j^\downarrow \frac{\partial S}{\partial \xi} \frac{\partial \xi}{\partial z} \quad (17)$$

325

326 Rearranging Equation 17:

327

$$328 \quad -\bar{D} \left[\frac{\partial^2 S}{\partial \xi^2} \left(\frac{\partial \xi}{\partial z} \right)^2 + \frac{\partial S}{\partial \xi} \frac{\partial^2 \xi}{\partial z^2} \right] - br_j^\downarrow \frac{\partial S}{\partial \xi} \frac{\partial \xi}{\partial z} + \phi \frac{\partial S}{\partial \xi} \frac{\partial \xi}{\partial t} = -\frac{\rho_{\text{ice}}}{\rho_{\text{br}}} S \frac{\partial \phi}{\partial \xi} \frac{\partial \xi}{\partial t} \quad (18)$$

329

330 Taking the appropriate spatial and temporal derivatives of ξ and substituting their values into
 331 Equation 18 gives:

$$332 \quad -\bar{D} \frac{\partial^2 S}{\partial \xi^2} - (br_j^\downarrow + \phi v_m(t)) \frac{\partial S}{\partial \xi} = v_m(t) \frac{\rho_{\text{ice}}}{\rho_{\text{br}}} S \frac{\partial \phi}{\partial \xi} \quad (19)$$

334
 335 For simplicity, we assume that $\phi(\xi) = \mathcal{H}(\xi)$, where $\mathcal{H}(\xi)$ is the Heaviside step function. While
 336 this is indeed a simplification, as it represents the mushy layer as an infinitesimally thin regime,
 337 the general liquid fraction profile of evolving sea ice demonstrates similar structure (See Figures
 338 5-7 of Buffo et al., 2018). Substituting $\phi(\xi) = \mathcal{H}(\xi)$ into Equation 19 results in a simplified
 339 conservation of mass equation in the moving coordinate system:

$$340 \quad -\bar{D} \frac{\partial^2 S}{\partial \xi^2} - (br_j^\downarrow + \phi v_m(t)) \frac{\partial S}{\partial \xi} = v_m(t) \frac{\rho_{\text{ice}}}{\rho_{\text{br}}} S \delta(\xi) \quad (20)$$

341
 342 where $\delta(\xi)$ is the delta function. Equation 20 can be solved using Fourier transforms. Let the
 343 transform variable be χ , such that:

$$344 \quad S(\chi) = \mathcal{FT}[S(\xi)] = \int_{-\infty}^{\infty} S(\xi) \exp(-i2\pi\chi\xi) d\xi \quad (21)$$

$$345 \quad S(\xi) = \mathcal{FT}^{-1}[S(\chi)] = \int_{-\infty}^{\infty} S(\chi) \exp(i2\pi\chi\xi) d\chi \quad (22)$$

346
 347 Applying the Fourier transform to Equation 20 gives:

$$348 \quad 4\pi^2 \chi^2 \bar{D} S(\chi) - i2\pi\chi (br_j^\downarrow + \phi v_m(t)) S(\chi) = v_m(t) \frac{\rho_{\text{ice}}}{\rho_{\text{br}}} S(\xi = 0, t) \quad (23)$$

349
 350 Equation 23 has the solution:

$$351 \quad S(\chi) = S(\chi, t) = \frac{v_m(t) \frac{\rho_{\text{ice}}}{\rho_{\text{br}}} S(\xi = 0, t)}{4\pi^2 \chi^2 \bar{D} - i2\pi\chi (br_j^\downarrow + \phi v_m(t))} \quad (24)$$

352
 353 Taking the inverse Fourier transform of Equation 24 gives:

$$354 \quad S(\xi, t) = \int_{-\infty}^{\infty} \left[\frac{v_m(t) \frac{\rho_{\text{ice}}}{\rho_{\text{br}}} S(\xi = 0, t)}{4\pi^2 \chi^2 \bar{D} - i2\pi\chi (br_j^\downarrow + \phi v_m(t))} \right] \exp(i2\pi\chi\xi) d\chi \quad (25)$$

$$355 \quad = \frac{v_m(t) \frac{\rho_{\text{ice}}}{\rho_{\text{br}}} S(\xi = 0, t)}{(br_j^\downarrow + \phi v_m(t))} \left[\pm 1 \mp \exp\left(\frac{-\pi\xi (br_j^\downarrow + \phi v_m(t))}{\bar{D}}\right) \right] \quad (26)$$

363
 364 Throughout this work we seek constitutive equations that relate the amount of salt entrained in
 365 forming ice to depth and local thermal gradient. Using the relationships of Equations 11 & 15, the
 366 definition of $\xi = z - z_m(t)$, and assuming in the active mushy layer near the ice-ocean interface,
 367 where reactive transport is possible, $z \sim z_m(t)$, we can rewrite Equation 26 in two forms:

$$369 \quad S_{\text{tot}}(z_m) \propto \frac{1}{z_m} [1 - \exp(-z_m)] \quad (27)$$

$$370 \quad S_{\text{tot}} \left(\frac{\partial T}{\partial z} \right) \propto \frac{\frac{\partial T}{\partial z}}{1 + \frac{\partial T}{\partial z}} \left[1 - \exp \left(-1 / \frac{\partial T}{\partial z} \right) \right] \quad (28)$$

372
 373 where the first term on the right-hand side of each equation is a diffusion term which dominates at
 374 later times (deeper depths, lower thermal gradients) and the second term is an advection-reaction
 375 term which dominates at early times (shallower depths, larger thermal gradients). Together,
 376 Equations 27 & 28 provide the functional forms for the constitutive equations produced throughout
 377 the remainder of the text.

378 2.3 The Europa Environment

380 Aside from the different surface temperature (<110 K vs ~250 K), gravity (1.32 vs 9.81
 381 m/s²) and potential compositional characteristics between Europa and Earth, one of the largest
 382 differences is sheer scale of the ice. While the majority of sea ice exhibits a maximum thickness
 383 of <10 m [Kurtz and Markus, 2012; Laxon et al., 2013] (ice drafts have been known to exceed 25
 384 m and reach up to 47 m beneath pressure ridges [Davis and Wadhams, 1995; Lyon, 1961]) and
 385 marine ice accretion occurs at depths <1.5 km [Craven et al., 2009; Galton - Fenzi et al., 2012;
 386 Zotikov et al., 1980], Europa's ice shell is likely ~10->30 km thick [Billings and Kattenhorn, 2005;
 387 Nimmo et al., 2003; Tobie et al., 2003]. It is important to note, however, that despite differences
 388 in ice thickness, all ice-ocean interfaces will remain at or near their pressure melting points, which
 389 for a 1.5 km thick terrestrial ice shelf is comparable to an ~11 km thick European ice shell.

390 To explore the end member states where high salinity ice is possible, model runs are
 391 initiated with the domain completely filled by one of the ocean chemistries investigated at a
 392 temperature just above its freezing point (Supplementary Section S1). The top boundary is
 393 governed by a Neumann boundary condition with a no-flux condition set for salt and it is assumed
 394 that the overlying ice is in conductive thermal equilibrium [McKinnon, 1999] (i.e. $dT/dz =$
 395 $(T_{oc} - T_s)/H_{\text{shell}}$). This is a reasonable assumption as the Stefan number for the ice-ocean system
 396 ($St = c_{\text{ice}}(T_{oc} - T_s)/L_f$), which compares sensible and latent heat, is small (<1.04) for all cases
 397 considered here (See Figure 3 of Huber et al. [2008]). The bottom boundary is governed by a
 398 Dirichlet boundary condition and is simulated as being in contact with an infinite ambient
 399 ocean/brine reservoir ($T_{oc}, S_{oc}, \rho_{sw}$) (for additional information on code functionality see [Buffo et
 400 al., 2018]). This arrangement results in the propagation of a solidification front from the
 401 undercooled upper boundary, which represents the extreme endmember of the initial
 402 crystallization of Europa's ice shell from an outer ocean layer (e.g. [Bhatia and Sahijpal, 2017;
 403 Bierson et al., 2020; Manga and Wang, 2007]). Such a model allows us to explore the ice shell
 404 thicknesses, and thus thermal gradients, at which impurity entrainment stabilizes and define the

405 properties of the ice across many regimes; a valuable metric given that Europa's ice shell likely
 406 experienced episodic thinning and thickening (e.g. [Doggett *et al.*, 2009; Figueredo and Greeley,
 407 2004; Hussmann *et al.*, 2002; Leonard *et al.*, 2018]).

408 To construct the full ice shell from discrete model runs, several simulations at various
 409 depths (solidification front locations) run in parallel, and the results are combined to produce the
 410 constitutive relationships that relate ice composition to its thermochemical environment at the time
 411 of formation. It is important to note that the top-down unidirectional solidification of Europa's ice
 412 shell from a quiescent ocean is likely a simplification as the aqueous differentiation of its juvenile
 413 planetesimal was likely a tumultuous and complex process [Kargel *et al.*, 2000]. We do not seek
 414 to investigate a specific thermal history of Europa's ice shell, rather our chosen formation scenario
 415 allows us to investigate a wide range of conditions and thermal regimes at once, and mirrors the
 416 formation of sea and marine ice, the only benchmarks available for the formation of ocean-derived
 417 ices. Thereby this model provides the simplest case that enables the derivation of the upper limit
 418 of salt possible in Europa's ice shell. Moreover, the functional forms of the constitutive equations
 419 are derived under such conditions, requiring simulations of this type to derive the bulk salinity-
 420 thermal gradient relationships paramount to the remainder of the manuscript (e.g. basal fracture
 421 and perched lens solidification).

422 Composition of the ocean is critical to ice formation because of the relationship between
 423 the salinity of water and its freezing point. The conductive nature of Europa's ocean [Khurana *et*
 424 *al.*, 1998; Kivelson *et al.*, 2000], as well as spectral measurements [McCord *et al.*, 1999], suggests
 425 the presence of dissolved salts, but nearly all of its intrinsic properties (thickness, composition,
 426 structure) remain poorly constrained. Potential European ocean chemistries have been explored in
 427 a number of studies [Marion *et al.*, 2005; McKinnon and Zolensky, 2003; Vance *et al.*, 2019;
 428 Zolotov and Kargel, 2009; Zolotov and Shock, 2001]. Here we implement the chemistry proposed
 429 by Zolotov and Shock [2001], who assumed that Europa's ocean formed during its differentiation
 430 via partial aqueous extraction from bulk rock with the composition of CV carbonaceous chondrites
 431 (Table 2). Alternate formation materials (e.g. CI chondrites [Zolotov and Kargel, 2009]) will alter
 432 the predicted ionic composition of the ocean, and variable molecular diffusivities, atomic masses,
 433 and van't Hoff factors may affect impurity entrainment rates in associated ocean-derived ices. For
 434 comparison, we also considered an ocean composition identical to terrestrial seawater (Table 2).
 435 Well-known liquidus curves exist for terrestrial seawater [IOC, 2015]. However, the freezing
 436 behavior of potentially more exotic European ocean compositions is comparatively less well known,
 437 so we constructed a new software package, Liquidus 1.0, to derive quadratic liquidus curves for
 438 any chemistry supported by the equilibrium chemistry package FREZCHEM 6.2, which includes
 439 a wide range of material properties for the expected non-ice components of brines (Supplementary
 440 Section S1).

441

Species	Terrestrial Seawater (mol/kg)	European Ocean (mol/kg)
Na ⁺	4.69 x 10 ⁻¹	4.91 x 10 ⁻²
K ⁺	1.02 x 10 ⁻²	1.96 x 10 ⁻³
Ca ²⁺	1.03 x 10 ⁻²	9.64 x 10 ⁻³
Mg ²⁺	5.28 x 10 ⁻²	6.27 x 10 ⁻²
Cl ⁻	5.46 x 10 ⁻¹	2.09 x 10 ⁻²
SO ₄ ²⁻	2.82 x 10 ⁻²	8.74 x 10 ⁻²
Total Salt (ppt)	34	12.3

442 **Table 2 – Ocean compositions.** List of ion species and relative abundances for terrestrial seawater [*Dickson and*
443 *Goyet, 1994*] and the proposed European ocean chemistry of [*Zolotov and Shock, 2001*].

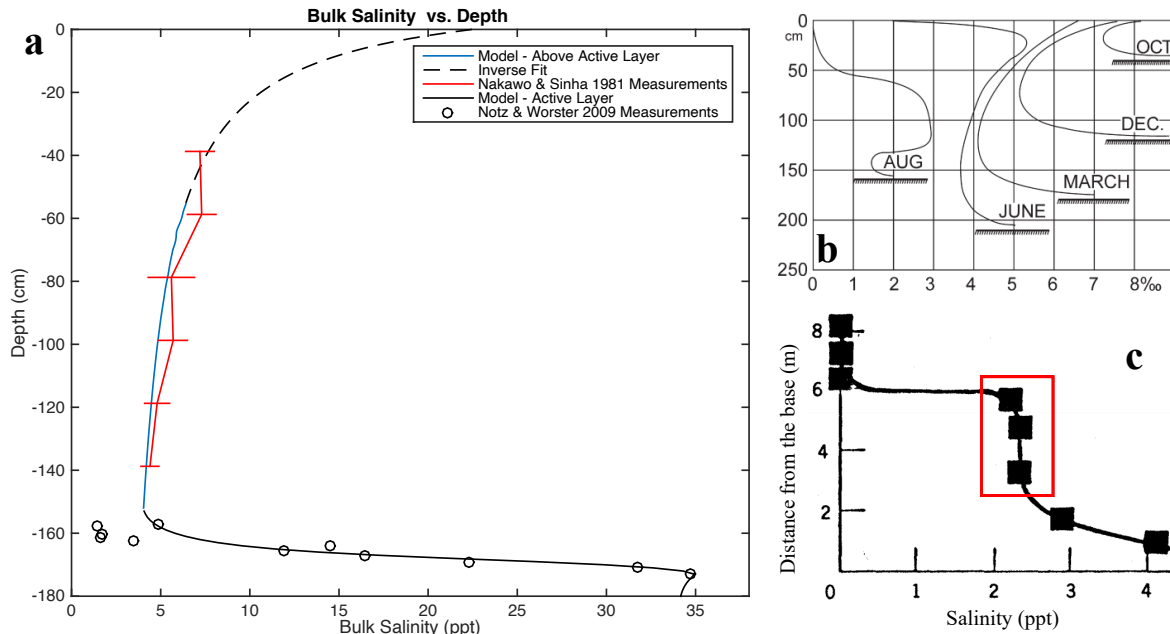
444
445 We forego simulating the possible precipitation of hydrated salts (e.g. mirabilite ($\text{Na}_2\text{SO}_4 \cdot$
446 $10\text{H}_2\text{O}$) [*Butler et al., 2016*], epsomite ($\text{MgSO}_4 \cdot 7\text{H}_2\text{O}$), meridianiite ($\text{MgSO}_4 \cdot 11\text{H}_2\text{O}$)
447 [*McCarthy et al., 2011; McCarthy et al., 2007*]) for two reasons. First, implementing reactive
448 transport modeling to simulate the evolution of ice-ocean worlds is a relatively novel approach,
449 thus it is logical to begin with the simpler ice-brine binary system (as opposed to the ice-brine-
450 hydrate ternary system), to both validate the approach and obtain a first order understanding of
451 how salts are entrained in planetary ices. Second, the low thermal gradients experienced
452 throughout much of the shell will facilitate slow ice growth, allowing for the dissipation of salt
453 from high salinity regions via both convection and diffusion, preventing saturation and
454 precipitation. Future work investigating ternary systems could reveal additional bulk salinity
455 profile structure in the shallow ice shell and other high thermal gradient environments brought
456 about by the precipitation of such hydrated salts. We discuss the potential geophysical implications
457 of salt hydrates in the context of intrusive hydrological features (basal fractures and perched water
458 bodies) in Sections 3.3.2 and 3.3.3.

459 **3. Results**

460 **3.1 Salt Entrainment on Earth**

461
462 Two types of ice present on Earth provide the best end-member analogs for Europa’s ice
463 shell: sea ice and marine ice. Here, sea ice refers to frozen seawater at the ocean’s surface, while
464 marine ice is seawater-derived ice which has accreted onto the basal surface of meteoric ice shelves
465 (e.g. [*Zotikov et al., 1980*]). While both ices form via the directional solidification of seawater, and
466 thus undergo the same dynamics during their formation, they form under different thermal regimes,
467 resulting in disparate compositional and physical structure. Sea ice provides the upper limit of
468 impurity entrainment and an ideal analog for ice formed along steep thermal gradients near
469 Europa’s surface, as its formation is driven by rapid heat loss to the cold polar atmosphere.
470 Fortunately, there exists nigh on a century’s worth of observations and quantitative measurements
471 regarding vertical heterogeneities in the thermal, chemical, and microstructural properties of sea
472 ice [*Malmgren, 1927*]. With the proximity of the 100 K surface, Europa’s shallow ice shell (< 1
473 km) and any shallow liquid water bodies emplaced at such depths within the shell will experience
474 similarly high thermal gradients (e.g. [*Chivers et al., 2020; Chivers et al., 2019; Michaut and*
475 *Manga, 2014*]), suggesting high impurity uptake exceeding even that of sea ice. We have
476 previously modeled the growth of sea ice to study its thermochemical evolution and ability to
477 record variations in ocean characteristics through the reproduction of ice core properties [*Buffo et*
478 *al., 2018*]. This model was adapted to actively track the advancing ice-ocean interface and
479 accommodate potentially diverse ocean chemistries. In Figure 3, we re-validate our approach by
480 comparing sea ice simulations to empirical measurements of depth dependent sea ice bulk salinity
481 [*Nakawo and Sinha, 1981; Notz and Worster, 2009*]. We show that actively tracking the evolution
482 of the ice-ocean interface and simulating small-scale solute transport within the porous ice
483 produces bulk salinity profiles that agree well with observations. We achieve salinity profiles that
484 exhibit the characteristic ‘c-shape’ typical of first-year sea ice, represented by the ‘MARCH’
485 profile of Figure 3b [*Malmgren, 1927*], and reproduce the bulk salinity values observed in the
486 field. Based on the constitutive relationship between depth and bulk salinity (Eq. 10), we use an
487 inverse fit to the simulated values to extend the profile to the upper portion of the ice where extreme
488 temperature gradients affect numerical stability when using a Neumann boundary condition. Thus,

489 our model captures the physical processes that occur during ice formation in high thermal gradient
 490 environments, which will govern the formation of ice near Europa's surface. This is relevant to
 491 both a young, thin ice shell, episodes of thinning, and any contemporary water bodies in the
 492 shallow subsurface.
 493



494 **Figure 3: Salinity profiles within observed and modeled marine and sea ice. a)** Modeled (blue and black solid
 495 lines), empirical (red line [Nakawo and Sinha, 1981] and black circles [Notz and Worster, 2009]), and inverse fit
 496 (black dashed line) bulk salinity profiles of sea ice. The numerical model assumes a preexisting 50 cm thick layer of
 497 sea ice in conductive equilibrium (linear temperature profile) with an atmospheric temperature of 250K and an ocean
 498 temperature of 271.5K. A conductive heat flux is maintained throughout the simulation at the upper boundary. The
 499 model was run for 1.5×10^7 sec (~ 174 days, a typical sea ice annual cycle) with a time step of 100 sec. The dashed line
 500 is the product of a Levenberg-Marquardt algorithm fit to the function $S(z) = a + b/(c - z)$, where S is bulk salinity, z is
 501 depth, and a , b , and c are constants, applied to the modeled bulk salinities above the active layer (blue solid line).
 502 While all of the bulk salinity values (blue and black solid lines) are a byproduct of the same model simulation, values
 503 in the active layer (black solid line) are excluded from the Levenberg-Marquardt fit (black dashed line) as the
 504 constitutive equations (Table 3) are derived assuming an infinitesimally thin mushy layer. **b)** Typical first-year sea ice
 505 salinity profiles have a characteristic 'c' shape where the bulk salinity evolves over the season due to material transport
 506 and ice growth (from [Malmgren, 1927]). **c)** Bulk salinity measurements from the bottom 8 m of an ice core extracted
 507 from the Ross Ice Shelf by [Zotikov et al., 1980]. The bottom 6 m is accreted marine ice, with the 'asymptotic region'
 508 outlined in red approaching diffusive equilibrium during ice formation (image modified from [Zotikov et al., 1980]).
 509

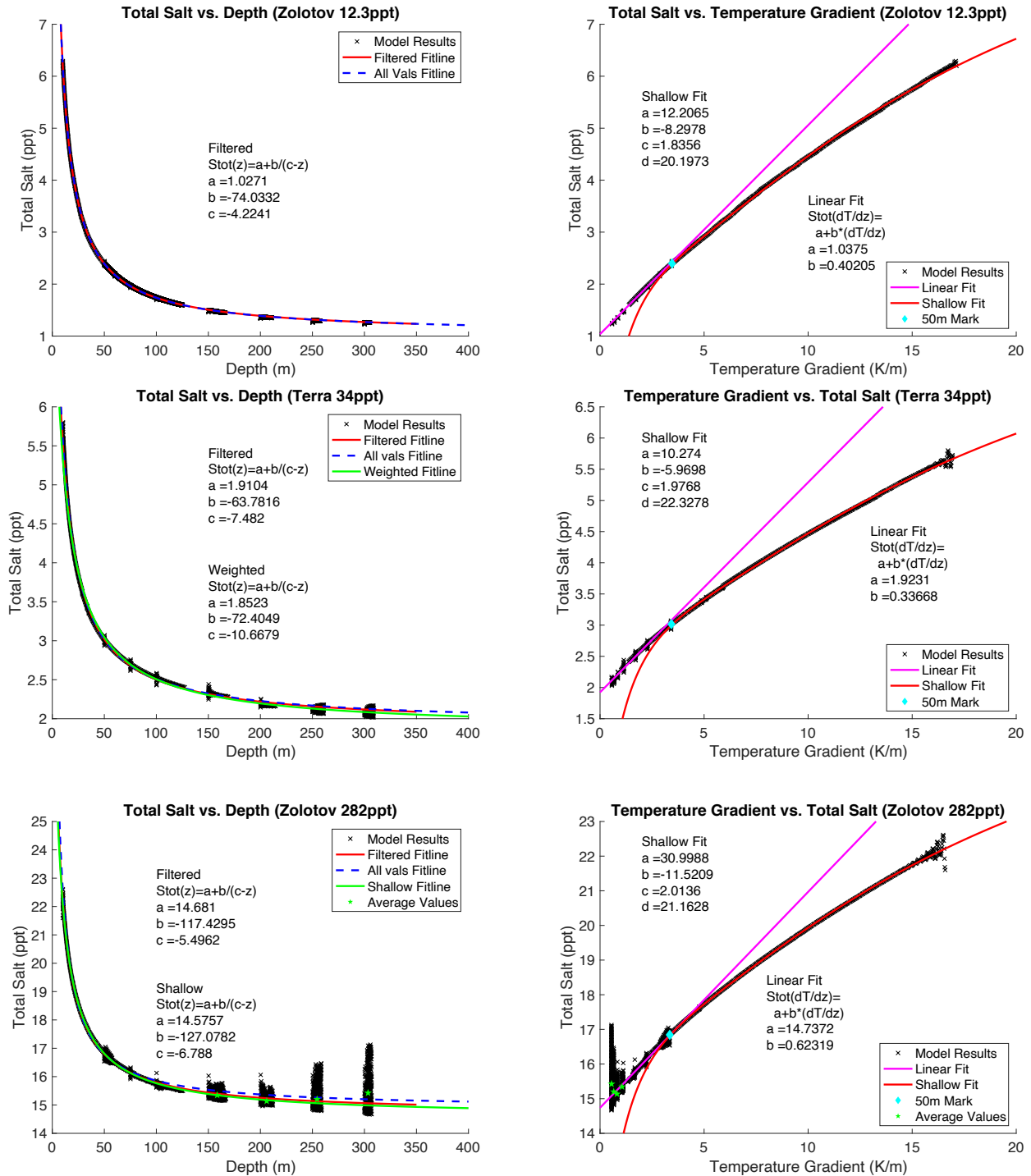
510 Most of Europa's ice shell (below about 1 km), however, will have formed and evolved
 511 under low thermal gradient conditions. As thermal gradients decrease, ice composition approaches
 512 an asymptotic lower limit governed by the critical porosity of the active layer when it is in diffusive
 513 equilibrium with the underlying ocean, as demonstrated below for the case of marine ice accreting
 514 beneath the Ross Ice Shelf. Here, critical porosity is analogous to a percolation threshold, where
 515 regions with porosities below this limit are no longer hydraulically connected to the surrounding
 516 pore network and any remaining salt is trapped in discrete brine pockets. A similar environment
 517 to the bulk of Europa's ice shell exists at the base of deep ice on Earth where marine ice is formed
 518 (e.g. [Zotikov et al., 1980]). This unique, and less studied, variety of ocean-derived ice forms on
 519 the basal surface of terrestrial ice shelves due to much lower thermal gradients than typical open
 520 ocean sea ice (e.g. ~ 10 K/m for surficial sea ice; ~ 0.08 K/m for marine ice [Zotikov et al., 1980])

521 leading to greatly reduced growth rates of ~ 2 cm/yr [Zotikov *et al.*, 1980]. While the thermal
 522 gradients present in the marine ice system (~ 0.08 K/m) exceed the upper estimates for a thin (5-10
 523 km) European ice shell (~ 0.02 K/m) [McKinnon, 1999; Mitri and Showman, 2005], even at this
 524 higher thermal gradient impurity entrainment has already approached its lower limit –
 525 characterized by asymptotic bulk salinity profiles, shown in Figure 3c. This makes marine ice the
 526 best terrestrial analog of European ice formed in the low thermal gradient regime. Adopting a
 527 critical porosity of $\phi_c = 0.05$, based on observations of sea ice permeability [Golden *et al.*, 1998;
 528 Golden *et al.*, 2007], and assuming an ocean salinity, $S_{oc} = 34$ ppt, the theoretical lower limit for
 529 salt entrainment into terrestrial ice (diffusive equilibrium when impermeability is reached) is given
 530 by $S_{lim} = \phi_c S_{oc} = 1.70$ ppt. The average bulk salinity of the ‘asymptotic region’ seen in Figure
 531 3c is 2.32 ppt. Utilizing the constitutive equation for bulk salinity versus thermal gradient derived
 532 in the next section for terrestrial seawater in the diffusive regime ($dT/dz = 0.08$ K/m), a bulk
 533 salinity of 1.95 ppt is predicted. The difference of 0.37 ppt between the observed and predicted
 534 bulk salinity values translates to a 16% error, attributed to small variations in unconstrained
 535 parameters, such as critical porosity and permeability-porosity relationships (both of which can
 536 appreciably affect impurity entrainment rates [Buffo *et al.*, 2018]). The efficiency of brine
 537 migration through the porous ice lattice and the threshold at which percolation is possible are
 538 poorly constrained [Golden *et al.*, 1998; Golden *et al.*, 2007; Wells *et al.*, 2011] but govern the
 539 dynamics of multiphase flow, brine retention in the ice, and ultimately ice composition. At the ice-
 540 ocean/brine interface, reduced permeability or a larger critical porosity would lead to more salt
 541 being entrained in the ice. Alternately, enhanced permeability, a smaller critical porosity, or the
 542 dearth of a percolation threshold (e.g. due to melt transport along ice grain boundaries [McCarthy
 543 *et al.*, 2013; McCarthy *et al.*, 2019]) would result in less salt entrainment. Nevertheless, our model
 544 closely reproduces observations of sea ice, and the same multiphase reactive transport physics
 545 applied in low-thermal gradient conditions match observations of marine ice composition, which
 546 capture broadly the two thermochemical regimes that ice on Europa is expected to occupy.

547

548 3.2 The Effects of Thermal Gradient and Ocean Chemistry on Ice Composition

549 We simulated Europa’s ice shell growth at eight discrete ice thicknesses to capture the full
 550 range of impurity entrainment possible (10 m, 50 m, 75 m, 100 m, 150 m, 200 m, 250 m, and 300
 551 m), for four different hypothetical ocean compositions (European Ocean 12.3 ppt/100 ppt/282 ppt
 552 and Terrestrial Seawater 34 ppt). We find that for ice thicknesses beyond 300 m the thermal
 553 gradient at the ice-ocean interface is shallow enough that the bulk salinity curve becomes
 554 asymptotic and variations in the salt entrainment rate will be minimal at all greater depths. This
 555 asymptotic lower limit is set by the ocean composition and critical porosity ($S_{lim} = \phi_c S_{oc}$). Direct
 556 simulations of larger ice thicknesses (>300 m) were therefore excluded, given the predicted ice
 557 composition below 300 m would vary by <1 ppt (see the first row of Table 3 and the following
 558 paragraph). European ocean concentrations were selected to bound the best estimates available from
 559 theory and observation: a rigorous estimate provided by theoretical calculations is 12.3 ppt
 560 [Zolotov and Shock, 2001], while the saturation point of the same fluid would reach an ocean
 561 salinity of 282 ppt, and the upper limit based on the Galileo magnetometer data is a salinity of 100
 562 ppt [Hand and Chyba, 2007]. The results for all ocean compositions can be seen in Figure 4 and
 563 Supplementary Figure S4. The results are depth-dependent and thermal gradient-dependent bulk
 564 salinity profiles, which are then interpolated using a Levenberg-Marquardt algorithm fit to the
 565 constitutive equations, the explicit form of which, including the coefficients needed to
 566 accommodate stretches and translations, are shown in Table 3.



567

Figure 4: Simulations of depth dependent and thermal gradient dependent bulk salinity for three different ocean chemistries (100 ppt simulation is presented in Figure S4) Relationships are fit by the constitutive equations of Table 3. **Left Column**, Model results [black exes] (numerical dispersion at the onset of each run has been removed) and original (all values), filtered (numerical dispersion at run onset removed), weighted (where applicable – weighted by data density), and shallow (where applicable – fitting model results from 10-200 m runs) fit lines [blue dashed line, red line, and green lines, respectively]. **Right Column**, Simulated results [black exes] as well as linear and ‘Shallow’ (See Table 3) fit lines [pink and red lines, respectively]. Green stars represent average bulk salinity for an entire run at a given depth – highlighting that the majority of the simulated data lies near the fit lines, even when scatter is

present. Blue diamonds identify the thermal gradient associated with a 50 m depth within an equilibrated conductive ice shell, which is the transition point between the diffusive and advective-reactive regimes.

Constitutive Equation	a	b	c	d
$S_{\text{tot}}(z) = a + \frac{b}{(c - z)}$	a _{12.3} =1.0271 a ₁₀₀ =5.38 a ₂₈₂ =14.681 a ₃₄ =1.8523	b _{12.3} =-74.0332 b ₁₀₀ =-135.096 b ₂₈₂ =-117.429 b ₃₄ =-72.4049	c _{12.3} =-4.2241 c ₁₀₀ =-8.2515 c ₂₈₂ =-5.4962 c ₃₄ =-10.6679	
$S_{\text{tot}}\left(\frac{\partial T}{\partial z}\right) = a + b \frac{\partial T}{\partial z}$	a _{12.3} =1.0375 a ₁₀₀ =5.4145 a ₂₈₂ =14.737 a ₃₄ =1.9231	b _{12.3} =0.40205 b ₁₀₀ =0.69992 b ₂₈₂ =0.62319 b ₃₄ =0.33668		
(Shallow Fit Line) $S_{\text{tot}}\left(\frac{\partial T}{\partial z}\right) = a + \frac{b\left(\frac{\partial T}{\partial z} + c\right)}{1 + \frac{\partial T}{\partial z}} \left[1 - \exp\left(\frac{-d}{\frac{\partial T}{\partial z}}\right)\right]$	a _{12.3} =12.21 a ₁₀₀ =22.19 a ₂₈₂ =31.00 a ₃₄ =10.27	b _{12.3} =-8.30 b ₁₀₀ =-11.98 b ₂₈₂ =-11.52 b ₃₄ =-5.97	c _{12.3} =1.836 c ₁₀₀ =1.942 c ₂₈₂ =2.014 c ₃₄ =1.977	d _{12.3} =20.20 d ₁₀₀ =21.91 d ₂₈₂ =21.16 d ₃₄ =22.33

568 **Table 3: Constitutive Equations.** The reactive transport model results are fit by constitutive equations relating bulk
569 salinity to shell depth and temperature gradient for each of the ocean compositions, column 1, and their associated
570 coefficients, a-d. Subscripts 12.3, 100, 282, and 34 refer to European ocean compositions with concentrations of 12.3
571 ppt, 100 ppt, 282 ppt, and terrestrial seawater with a concentration of 34 ppt, respectively. These equations provide a
572 parameterization of Europa's ice shell composition's dependence on the local thermal environment at the time of ice
573 formation, which can be utilized to provide efficient first order estimates of the properties of ice formed in a variety
574 of chemical and thermal environments without the need for explicit simulation.

575

576

577

578

579

580

581

582

583

584

585

586

587

588

589

590

591

592

593

594

595

596

597

598

599

600

The translation of the model from the Earth system to Europa hinges on the observation that as thermal gradients near the ice-ocean/brine interface decrease ice bulk salinity asymptotically approaches a lower limit governed by molecular diffusion in the pore fluid (Figure 3c). The result of this asymptotic behavior is twofold. First, the ice shell will experience ice-ocean interface thermal gradients below those found on Earth during much of its formation. This suggests a relatively homogeneous ice layer (formed in the asymptotic regime) underlying a thin (~1 km), compositionally distinct surficial layer (formed under steep thermal gradients). This stratification would produce variations in the thermochemical and mechanical properties of these layers, potentially introducing a boundary along which rheological transitions (e.g. brittle lid vs. ductile mantle) and transport regimes (conduction vs. convection) may be promoted. Second, the lower portion of the contemporary ice shell is believed to be ductile enough to undergo solid state convection [Barr and McKinnon, 2007; Han and Showman, 2005; McKinnon, 1999; Tobie et al., 2003], providing a mechanism that would mix this region of the shell, homogenizing it chemically and flattening its thermal profile (consider the analogous geothermal profile). A convective thermal profile in this ductile region suggests an ice-ocean interface subject to very low thermal gradients [Mitri and Showman, 2005], implying that accreted ice salinities would be at or near their lower limit, irrespective of ice thickness. Thus, the ductile region of the contemporary ice shell should have a bulk composition at or near the lower limit set by the critical porosity. Such a compositional profile varies negligibly from those predicted by the unidirectional solidification scenarios we simulate here (below 1 km predicted salinities vary by <150 ppm from the theoretical lower limit). Any heterogeneities in impurity entrainment would require associated ice-ocean heat flux variations (e.g., ocean driven heating of the ice shell [Soderlund et al., 2014], thermochemical diapirism [Pappalardo and Barr, 2004], spatiotemporal variations in basal heat flux due to downwelling cold ice and/or the evolution of tidal heating within the ice shell [Tobie et al., 2003]) with amplitudes large enough to appreciably affect entrainment rate. Notably, this implies that for

601 much of the ice shell it is not the thermal regime of the ice but rather its critical porosity and
602 permeability which will determine ice composition.

603 In general, the bulk salinity profiles and their corresponding relationships to depth within
604 the ice shell and local temperature gradients are well-represented by our derived constitutive
605 equations, suggesting that their functional forms (Eq. 27 & 28) capture much of the reactive
606 transport physics that govern how ice forms in the presence of dissolved materials, and the
607 movement of this material via advection and diffusion while the ice is still permeable. The division
608 of impurity entrainment rate into two distinct thermal regimes, diffusive (low) and advective-
609 reactive (high), is well accommodated and justified by the terrestrial benchmarks above. While
610 there exists uncertainties in the limit of extreme thermal gradients ($\gg 20$ K/m) and large salinities
611 (e.g. scatter observed for the 282 ppt ocean at low thermal gradients, a consequence of salinity's
612 increased sensitivity to changes in porosity at high ocean concentrations [Supplementary Section
613 S5]), the high thermal conductivity of ice relative to water quickly diffuses such thermal
614 anomalies. In conductive thermal equilibrium, 9 m of ice separating a 100 K surface and 273 K
615 ocean does not support thermal gradients in excess of 20 K/m. Thus, after a thin layer of ice (<10
616 m) has formed the ice-ocean interface is substantially insulated and the constitutive can be
617 confidently applied. Moreover, the results demonstrate that, as expected, the bulk salinity in the
618 ice approaches the diffusive equilibrium limit under low thermal gradients. Thus, as perhaps the
619 first quantitative estimate of impurity content, the constitutive equations derived here allow us to
620 investigate the properties and evolution of Europa's ice shell and hydrological features contained
621 therein.

622

623 3.3 The Evolution of Europa's Ice Shell

624 3.3.1 Total Salt

625 The constitutive equations derived above can be used to estimate the total salt content of
626 Europa's ice shell prior to the onset of solid-state convection, producing an upper limit on the total
627 impurity load of the ice shell. For these calculations, we assume a 25 km thick ice shell with an
628 inner radius of 1,535 km and an outer radius of 1,560 km. The total salt content for a given ocean
629 composition can be calculated by integrating the constitutive equation over the volume of the ice
630 shell given the coefficients in Table 3. For an ice shell with inner radius R_1 and outer radius R_2 ,

$$631 \quad \text{Total Salt in Shell} = \frac{\rho_{\text{ice}}}{1000} \int_V S_{\text{tot}}(z) dV \quad (28)$$

632

633 where ρ_{ice} is the density of ice, V is the volume of the ice shell, and $S_{\text{tot}}(z)$ is the constitutive
634 equation relating bulk salinity and depth (Table 3). Rewriting z in terms of the spherical coordinate
635 r , gives:

636

$$637 \quad \text{Total Salt in Shell} = \frac{\rho_{\text{ice}}}{1000} \int_{R_1}^{R_2} \int_0^{2\pi} \int_0^{\pi} \left[a + \frac{b}{(c - (R_2 - r))} \right] r^2 \sin \varphi \, dr \, d\theta \, d\varphi \quad (29)$$

638

639 where a , b , and c are coefficients from the ocean/brine specific constitutive equation and (r, θ, φ)
640 represent a spherical coordinate system.

641 The total volume of the 25 km thick European ice shell is $\sim 7.52 \times 10^{17} \text{ m}^3$, while the
642 approximate collective volume of Earth's oceans is $\sim 1.33 \times 10^{18} \text{ m}^3$ [Charette and Smith, 2010].

643 For the European ocean composition (Table 2), with concentrations of 12.3 ppt, 100 ppt, and 282
644 ppt the total salt entrained in a 25 km shell is 7.29×10^{17} kg, 3.66×10^{18} kg, and 1.02×10^{19} kg,
645 respectively. This corresponds to average ice shell salinities (total salt/ice shell mass) of 1.06 ppt,
646 5.31 ppt, and 14.8 ppt, respectively. For a terrestrial ocean composition with a concentration of 34
647 ppt the total salt entrained in a 25 km shell is 1.30×10^{18} kg, corresponding to an average ice shell
648 salinity of 1.88 ppt. For comparison, Earth's oceans contain $\sim 4.53 \times 10^{19}$ kg of salt.

649 Directly related to the composition and bulk salinity of the ice is its density. Crucial in
650 driving any potential solid-state convection on Europa, compositional buoyancy may either help
651 or hinder large scale, thermally driven convective overturn in the ice shell. Horizontal density
652 gradients have also been proposed as a driver of putatively observed subduction/subsumption on
653 Europa's surface [Johnson *et al.*, 2017a; Kattenhorn, 2018]. Mirroring the profiles of bulk salinity,
654 there exists a rapid and asymptotic decrease in ice density with depth for all ocean chemistries
655 (Supplementary Figure S5), and subsequently throughout much of the shell the density is nearly
656 homogeneous (e.g. for a 100 ppt European ocean chemistry $\rho_{500m}=922.54$ kg/m³ and
657 $\rho_{25km}=922.25$ kg/m³). Our results demonstrate that, apart from a geophysically thin surface layer,
658 significant variations in density with depth are unlikely to form as the ice shell freezes out. The
659 maximum salt content predicted in the near surface is ~ 36 ppt (or $\sim 3.6\%$), calculated by extending
660 the constitutive equation relating bulk salinity and shell depth for the 282 ppt ocean to the surface
661 ($z = 0$). The same calculation for the 100 ppt, 34 ppt, and 12.3 ppt oceans results in near surface
662 salt contents of ~ 22 ppt, ~ 9 ppt, and ~ 19 ppt (or $\sim 2.2\%$, $\sim 0.9\%$, and $\sim 1.9\%$), respectively. A
663 number of these values are greater than, or close to, the 2% salt content needed to drive the
664 subduction of certain laterally compositionally heterogeneous slabs calculated by [Johnson *et al.*,
665 2017b]. However, the physical, thermal, and chemical characteristics of the ice shell likely act in
666 concert to control Europa's dynamics, as the material properties of ice are structurally, thermally,
667 and chemically dependent (Supplementary Section S2). The expected salinity profile, along with
668 the total impurity load, provides context on the nature of liquid and solid phases within the ice
669 shell. Combined with thermal variations due to convection, tidal heating, or heat transfer from the
670 ocean [Howell and Pappalardo, 2018; Mitri and Showman, 2005] and variations in physical
671 properties such as porosity and viscosity [Barr and McKinnon, 2007; Johnson *et al.*, 2017b], more
672 explicit constraints on the thermophysical formation of many of Europa's surface features are thus
673 possible.

674

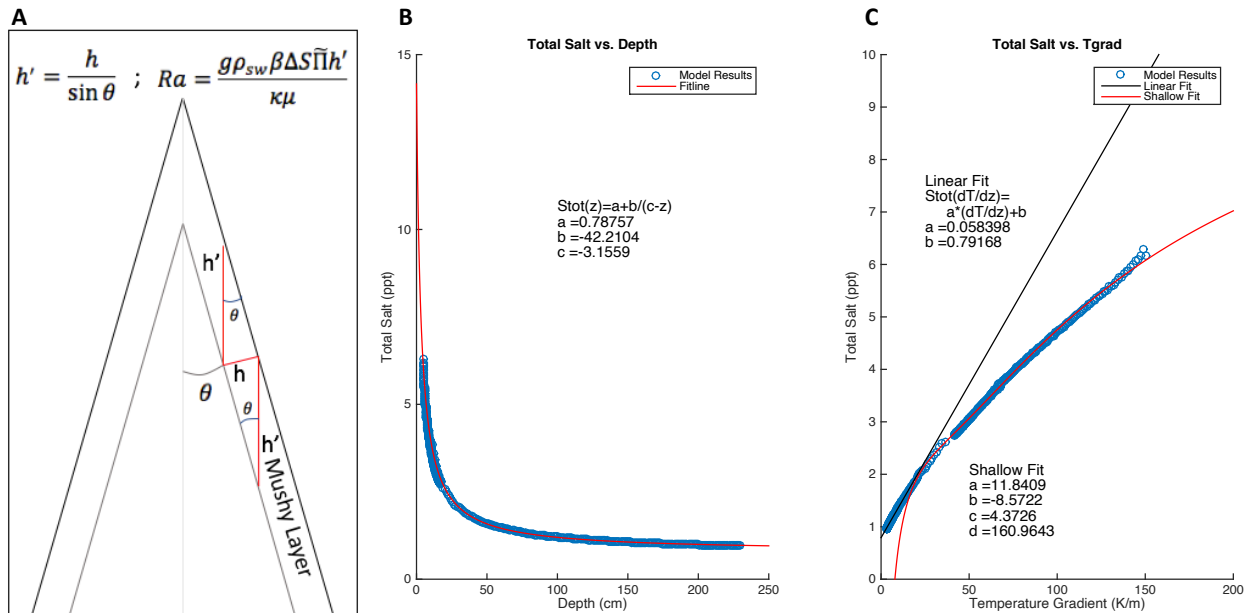
675 3.3.2 Basal Fractures

676 The fundamental processes that occur during the freezing of ice are not only applicable to
677 the ocean, but to any water within the ice shell. We adapted our approach to accommodate the
678 geometry and amplified gravity drainage of simple basal fractures (Figure 5a), to investigate the
679 composition of fractures upon re-freezing. Akin to the basal fractures of terrestrial ice shelves,
680 fractures at the ice-ocean or other ice-liquid interface of Europa could either locally stabilize or
681 destabilize the ice shell; they have the potential to suture the shell back together with newly frozen
682 oceanic material [Khazendar *et al.*, 2009], or to propagate further, potentially penetrating to the
683 surface [Bassis and Walker, 2012]. Such fractures appear within Europa's chaos terrain [Collins
684 and Nimmo, 2009; Walker and Schmidt, 2015], a potential indicator of near-surface water
685 reservoirs [Schmidt *et al.*, 2011] and a potential pathway for shallow water to make it to the surface
686 in the form of plumes [Sparks *et al.*, 2017] (See Figure 1a).

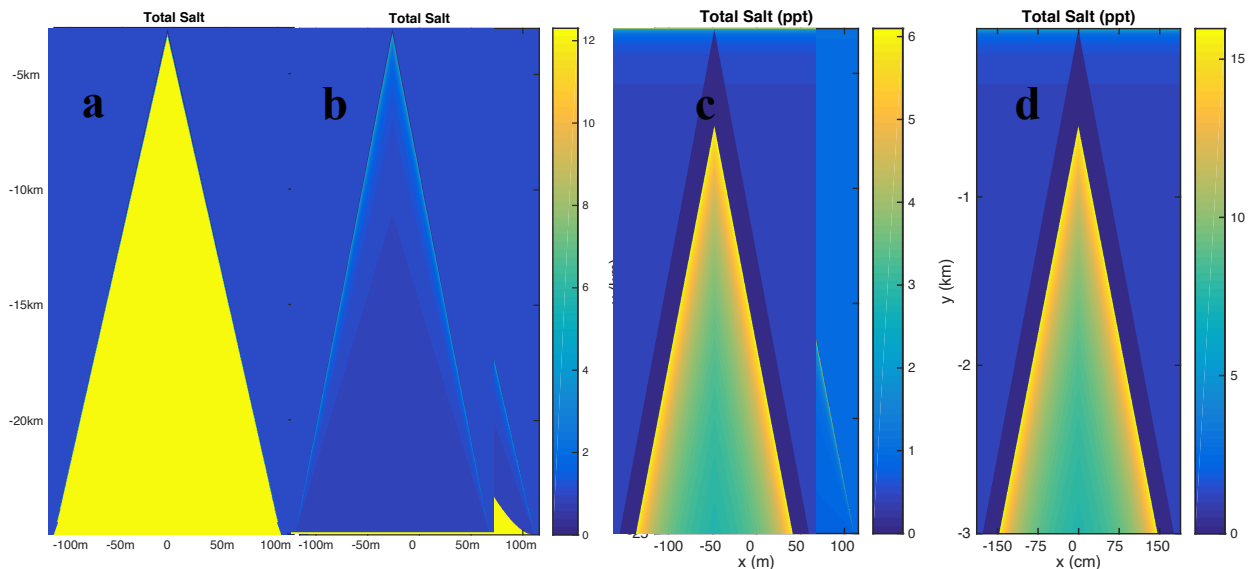
687 We modeled basal fractures at both Europa's ice-ocean interface and a hypothetical ice-
688 lens interface (Figure 6). The fractures are filled with fluid from the underlying reservoir (ocean

689 or lens) and the fluid is assumed to remain well mixed during the simulations since the advective
690 timescale for rejected brine with a density 1 kg m^{-3} greater than the ambient fluid through a 25 km
691 fracture is <1 day (equating gravitational and viscous drag forces for a parcel of brine near the
692 crack tip of width $\mathcal{O}(1)$, $v \sim \Delta \rho g / \eta$). Fracture geometries (penetration depth and basal width) are
693 calculated using the linear elastic fracture model of Walker et al. (2014) for ice with a tensile
694 strength of $0.1 \text{ MPa m}^{1/2}$ subject to an induced stress of 2MPa (Supplementary Section S3). New
695 constitutive equations were produced for each fracture geometry and ocean/brine composition
696 combination that account for the amplified gravity drainage in the fracture (an example can be
697 seen in Figure 5b-c). Due to the high aspect ratio of the basal fractures (penetration depth/basal
698 width) we modeled them as solidifying horizontally inward, akin to how terrestrial magmatic dikes
699 form, forced by the conductive profile of the ice shell into which the fracture is emplaced. Thermal
700 gradients at the fracture solidification front provide the inputs for the constitutive equations and
701 thus govern the salt content of the refreezing fracture. The injection of water into the ice shell
702 produces regions of very high thermal gradients between the relatively warmer water and cold ice.
703 As a result, fractures refreeze to form ice wedges with chemically graded composition, due to
704 the amplified solidification rates at the fracture's edges and tip. Bulk salinity estimates of the most
705 rapidly formed ice, near the walls of the fractures, have been excluded from Figure 6 (e.g. the dark
706 blue layer seen in panel 4d). Thermal gradients in this region are $> 20 \text{ K/m}$ and exceed the range
707 under which the majority of the constitutive equations were derived. Furthermore, under rapid
708 solidification there is the potential for salt hydrates to precipitate and be trapped within the ice
709 [McCord et al., 2002; Thomas et al., 2017], further altering its bulk salinity, thermophysical and
710 mechanical properties. Due to the complex and metastable evolution of hydrate precipitation [Chu
711 et al., 2016; Toner et al., 2014] we forego its simulation during the current investigation, but note
712 that the bulk salinity of the most distal ice is expected to approach that of the fluid filling the basal
713 fracture (i.e. increased salt retention upon flash freezing).

714 While these simulations do not completely capture all of the inherently two-dimensional
715 structure and ternary phase evolution of the fracture (especially near the crack tip) these results
716 currently provide the most realistic evaluation of basal fracture physicochemical evolution. The
717 results suggest that basal fractures are geologically short-lived (e.g. Figure 6a-b), at least in the
718 upper shell, due to their high aspect ratios and rapid heat loss to the surrounding ice. At depth their
719 lifetime may be extended by deformation processes brought about by tidal forces [Nimmo and
720 Gaidos, 2002] or the presence of a warmer ductile ice layer [Barr and McKinnon, 2007; Tobie et
721 al., 2003]. While it is unlikely that fractures in the shallow shell contain liquid water for long, we
722 show that the rapid injection and refreezing of saline fluid within a colder ice shell produces local
723 chemical heterogeneities along the fracture walls that could preserve the fracture. Two important
724 implications arise: the high salinity regions along the fracture walls produce a gradient in
725 mechanical properties, potentially weakening the center of the fracture or concentrating stress here,
726 while at the same time these regions could be more easily melted during reactivation of the fracture
727 even in the absence of water from the ocean. Both of these provide mechanisms by which features
728 can remain active even once they refreeze.



729
730 **Figure 5: Basal fracture geometry and constitutive relationships.** A) Basal fracture geometry, highlighting features
731 that are used to modify the gravity drainage parameterization. B-C) Model results (blue circles) and associated
732 constitutive equations (red and black lines) for a hypothetical ice-ocean interface basal fracture (12.3 ppt European
733 ocean, 1.125 km penetration depth, 11.34 m basal width).

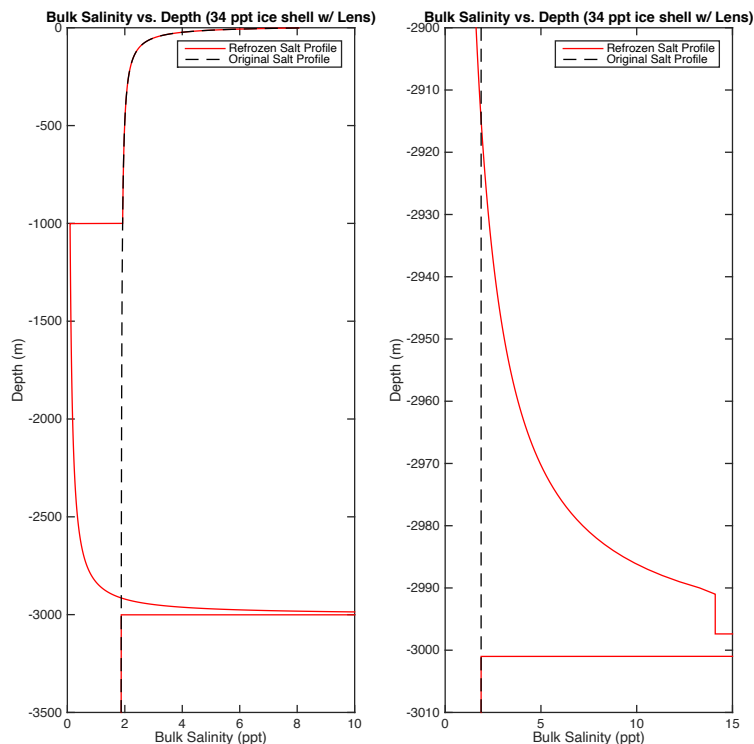


734 **Figure 6: Basal ice fractures refreeze to produce a gradient in salinity.** Temporal evolution of a hypothetical basal
735 fracture, a-b (Supplementary Figure S7 and Sections S3-4), shows that rapid refreezing occurs, down to 5km within
736 15 years if the fracture can be held open over this timeframe. Profiles for deep fractures from the ice-ocean interface,
737 c (due to 2 MPa stress in a 25 km shell; Depth - 21.925 km, Width - 220.9 m), and fractures from shallow lens
738 interfaces, d (due to 2 MPa stress in a 3 km lid, Depth - 2.922 km, Width - 3.53 m), show similar patterns of high salt
739 content along the fracture wall and toward the tip, and lower salinity toward the interior and base. These results show
740 that gradients in refrozen fracture mechanical properties are likely in the shallow shell where tidally modulated activity
741 is more probable. For fractures from the ocean, the majority of the ice formed in the interior of the fracture, however,
742 will have a salinity that is nearly indistinguishable from the bulk Europa ice. This suggests that fractures are likely to
743 be regions of local discontinuities in ice shell properties, and potentially regions of weakness within the ice shell
744 created by interfaces between salt and ice grains.

745

746 *3.3.3 Solidification of Shallow Water Bodies*

747 Knowing the composition of the ice provides the chance to evaluate the formation,
 748 evolution, and longevity of water or brine systems within Europa's ice shell. For example, shallow
 749 lenses of liquid water are suggested to form *in situ* via melting of the ice shell [Schmidt *et al.*,
 750 2011; Vilella *et al.*, 2020] (Figure 1a) or by injection through diking processes [Manga and
 751 Michaut, 2017; Michaut and Manga, 2014]. Here we investigate the salinity profile produced when
 752 a lens formed via *in situ* melting within a shell originally derived from a 34 ppt terrestrial ocean
 753 chemistry refreezes. We assume the lens is 2 km thick and its upper surface is located 1 km beneath
 754 the 100 K ice shell surface. We assume the lens freezes from the top down driven by a conductive
 755 thermal profile in the overlying ice (Neumann boundary condition such that $dT/dz =$
 756 $(T_{\text{lens}} - T_S)/H_{\text{roof}}$; where T_{lens} is the salinity dependent melting temperature of the lens [See
 757 Supplementary Section S1], and H_{roof} is the thickness of the ice overlying the lens). We have
 758 excluded bottom-up solidification of the lens, assuming an impinging warm diapir will limit
 759 bidirectional freezing. Letting the diffusive limit govern ice bulk salinity as shown above ($S_{\text{lim}} =$
 760 $\phi_c S_{\text{oc}}$) and tracking the evolving lens salinity, ice compositions ranging from 0.0946 to 14.10 ppt
 761 are produced (See Figure 7). Additionally, upon complete refreeze, impurity rejection leads to the
 762 precipitation of an approximately 2.23 m layer of salt (likely in the form of a salt hydrate),
 763 assuming a saturation limit of 282 ppt (Figure 7). This 'salting out' process during the freezing of
 764 eutectic brines has been observed in terrestrial systems (e.g. British Columbia's hypersaline lakes
 765 [Renaut and Long, 1989]), and provides an efficient segregation mechanism that results in
 766 relatively pure ice overlying saturated brine in which basal salt hydrate layers precipitate [Brown
 767 *et al.*, 2020; Buffo, 2019]. Additionally, our results are in good agreement with contemporary
 768 modeling studies investigating the two-dimensional thermochemical evolution of shallow water
 769 bodies on Europa [Chivers *et al.*, 2019].



770 **Figure 7: Bulk salinity profile of a perched water lens upon re-solidification. Left)** A 2 km thick lens, located 1
 771 km beneath Europa's surface (lens occupies 1-3 km), is assumed to form via the *in situ* melting of a preexisting ice
 772 shell, whose original composition is given by the black dashed line. Initially the lens salinity is less than that of the
 773 original ocean, but upon top down solidification salt is concentrated in the remaining liquid phase, leading to an
 774 increase in ice bulk salinity [red line] near the base of the refrozen lens as well as ~2.23 m of precipitated salt on the
 775 lens floor (1000 ppt values excluded from plot). **Right)** A magnified view of ice bulk salinity near the bottom of the
 776 lens (2.90 – 3.01 km). The lens saturates (282 ppt) when the ice reaches 2991 m, resulting in salt precipitation (2997.77
 777 – 3000 m).

778

779 4. Discussion

780 We have designed a multiphase reactive transport model that accurately simulates the
 781 complex dynamics of ice-ocean interfaces and applied it to the Europa system. We explicitly
 782 quantify the overall impurity content of Europa's ice shell, suggesting an average composition
 783 (total salt/ice shell mass) of between 1.053 and 14.72 ppt of non-ice material (depending on ocean
 784 composition). These results extend the general notion that Europa's ice shell contains ocean-
 785 derived impurities [Kargel *et al.*, 2000; Zolotov and Kargel, 2009] by providing two methods
 786 (direct modeling and constitutive equations) to predict the spatiotemporal distribution of salts
 787 within the shell. Our estimates of the ice shell's bulk salinity, predictions of concentrated salt layers
 788 near hydrological features within the shell, numerical models, and constitutive equations can be
 789 included in more realistic models of the geophysical evolution of the ice shell.

790 Compositional heterogeneities can either aid or prevent buoyancy driven convection in the
 791 ductile region of the ice shell, which is important for constraining the rates of subduction and
 792 surface recycling [Howell and Pappalardo, 2019; Johnson *et al.*, 2017a; Kattenhorn, 2018].
 793 Additionally, salts affect the rheological properties of the ice, especially relative to pure water ice,
 794 which impacts its mechanical behavior [Durham *et al.*, 2010; Durham *et al.*, 2005]. Estimates of
 795 material entrainment at the ice-ocean interface will aid in predicting the thermo-compositional
 796 convection dynamics in the ductile region of the shell (e.g. [Barr and McKinnon, 2007; Han and
 797 Showman, 2005; Pappalardo and Barr, 2004]) and help quantify ocean-surface material transport
 798 rates (e.g. [Allu Peddinti and McNamara, 2015]). These transport rates feed forward into the
 799 putative reductant-oxidant cycle associated with ocean-surface interaction [Vance *et al.*, 2016], by
 800 which ice shell overturn delivers surface-generated oxidants and ice-shell derived chemical species
 801 as potential energy sources to the ocean. Constraining chemical cycling associated with ice shell
 802 overturn and ocean-surface interaction is a fundamental component of assessing the habitability of
 803 Europa and other ice-ocean worlds [Des Marais *et al.*, 2008; Hendrix *et al.*, 2019; Pappalardo *et*
 804 *al.*, 2017; Schmidt, 2020].

805 Impurity entrainment and rejection during freezing produce compositional heterogeneities
 806 within the ice shell and introduce a concentration process capable of producing salt/salt hydrate
 807 layers that have highly distinct mechanical, thermal, and dielectric properties. Our results
 808 demonstrate regions of high material contrast associated with intrusive features within the ice shell
 809 that could promote or extend geologic activity and provide an observable indicator of past or
 810 present liquid environments. We have shown that the rate of ice formation is directly related to the
 811 entrainment of salts, suggesting that when fluids intruded into the ice shell contact the cold
 812 surrounding ice, they will form rinds of high salinity ice. These highly distinct layers will have
 813 fundamentally different thermal and mechanical properties than the background ice shell, making
 814 them susceptible to reactivation through stress concentration or eutectic melting. Quantifying
 815 compositional heterogeneities associated with hydrofracturing will improve estimates of fracture
 816 mechanics on Europa (e.g. [Craft *et al.*, 2016; Walker *et al.*, 2014]) and aid in determining if
 817 frictionally generated melts can be produced in active fractures (e.g. [Kalousová *et al.*, 2014;

818 2016]) by informing physicochemical and structural models of these features. Impurity rejection
819 from forming ice leads to the concentration of isolated hydrological features within the shell, such
820 as lenses, to the point that they can reach their saturation limit and precipitate layers of pure
821 hydrated salts. Our estimates of lens evolution (Section 3.3.3) include the chemical evolution of
822 the water bodies and can be used to improve estimates of their longevity (e.g. [Chivers *et al.*, 2020;
823 Michaut and Manga, 2014]) and habitability [Schmidt, 2020], as the composition of the fluid
824 impacts both the freezing point of the fluid and biologically important properties such as water
825 activity and chaotropicity [Oren, 2013; Pontefract *et al.*, 2019; Pontefract *et al.*, 2017].
826 Additionally, coupling predictions of impurity entrainment with contemporary solution
827 fractionation models will determine if certain ocean components are preferentially incorporated
828 into or excluded from the shell, revealing the detailed chemical structure of icy worlds and
829 identifying any enrichments or depletions of import (e.g. [Vance *et al.*, 2019; Zolotov *et al.*, 2004]).
830 Determining the lifetime and composition of liquid water features within the ice shell is of
831 profound importance in considering whether such reservoirs could be putative habitats; relevant
832 for both planetary exploration and planetary protection [NRC, 2012; Schmidt, 2020]. While our
833 models suggest that shallow subsurface water in a conductive ice shell is short lived, the warmer,
834 isothermal regime of an ice shell undergoing convection may provide an environment where
835 hydrological features could persist for much longer.

836 The ability to predict compositional variations around putative hydrological features in
837 Europa's shell will both constrain how these features form and inform spacecraft observations
838 [Blankenship *et al.*, 2009; Kalousova *et al.*, 2017]. The high salt contents associated with both
839 fractures and lenses make them prime candidates for detection by ice penetrating radar instruments
840 (e.g. RIME onboard JUICE, REASON onboard Europa Clipper [Plaut, 2019]), as salt substantially
841 alters the dielectric properties of ice (e.g. [Blankenship *et al.*, 2009; Schroeder *et al.*, 2016]). Our
842 model's ability to simulate the physicochemical evolution of the ice that forms in and around
843 hydrological features provides a means to predict the dielectric structure of both the features and
844 background ice shell. These dielectric profiles can be used as an inversion tool (e.g. [Kalousova *et al.*, 2017])
845 once radar observations have been made to constrain the structure, composition, and
846 evolution of remnant and relict hydrological features.

847

848 5. Conclusion

849 The impurity load and distribution of entrained ocean materials within Europa's ice shell
850 impacts the evolution of the ice shell, Europa's geology, and interactions between the surface and
851 the ocean. Compositional profiles of the bulk ice shell and geologic features effectively capture
852 the thermal and physicochemical nature of the ice that can be observed by Europa Clipper's remote
853 sensing and radar instruments: the spatial distribution of impurities on the surface and the dielectric
854 properties of the ice and water within the shell carry with them an accessible fingerprint of ice
855 shell dynamics and the ocean below. In addressing systems science level objectives (e.g.
856 habitability assessment [Pappalardo *et al.*, 2017]) future work combining the dynamics of material
857 entrainment with detailed ice-ocean world thermochemical models (e.g. [Journaux *et al.*, 2020;
858 McDougall and Barker, 2011; Neveu *et al.*, 2017]) and ice shell geodynamic and tectonic models
859 (e.g. [Howell and Pappalardo, 2019; Weller *et al.*, 2019]), promises to improve our understanding
860 of Europa's geophysics and habitability through the interpretation and synthesis of Europa Clipper
861 and JUICE observations.

862

863

864 **Acknowledgments**

865 **General**

866 The authors thank Sven Simon (Georgia Institute of Technology) for helpful discussions regarding
867 the analytical solution of the modified Stefan Problem.

868

869 **Funding**

870 This study was supported by the NASA Earth and Space Science Fellowship, grant NNX16AP43H
871 S01 and NNX16AP43H S002. Britney Schmidt was additionally supported by the Europa Clipper
872 Mission. Resources supporting this work were provided by the NASA High-End Computing
873 (HEC) Program through the NASA Advanced Supercomputing (NAS) Division at Ames Research
874 Center.

875

876 **Author Contributions**

877 J. J. B. contributed in designing the research, constructing the multiphase reactive transport model,
878 carrying out the research, interpreting the results, and writing/reviewing the paper.

879 B. E. S. contributed in designing the research, interpreting the results, and writing/reviewing the
880 paper.

881 C. H. contributed in constructing the multiphase reactive transport model, interpreting the results,
882 and writing/reviewing the paper.

883 C. C. W. contributed in constructing the fracture mechanics model, interpreting results, and
884 writing/reviewing the paper.

885

886 **Competing Interests**

887 The authors declare no competing financial nor non-financial interests.

888

889 **Materials and Correspondence**

890 *Code Availability*

891 Liquidus 1.0 and its associated documentation can be found in [Buffo, 2020a]

892 SlushFund 2.0 and its associated documentation can be found in [Buffo, 2020b]

893

894 All correspondence and material requests should be made to Jacob J. Buffo at:
895 jacob.j.buffo@dartmouth.edu

896

897

898

899

900

901

902

903

904

905

906

907

908

909

910 **References**

- 911 Allu Peddinti, D., and A. K. McNamara (2015), Material transport across Europa's ice shell,
 912 *Geophysical Research Letters*, 42(11), 4288-4293, doi:10.1002/2015GL063950.
- 913 Barr, A. C., and W. B. McKinnon (2007), Convection in ice I shells and mantles with self-
 914 consistent grain size, *Journal of Geophysical Research: Planets*, 112(E2),
 915 doi:10.1029/2006JE002781.
- 916 Bassis, J. N., and C. Walker (2012), Upper and lower limits on the stability of calving glaciers
 917 from the yield strength envelope of ice, *Proceedings of the Royal Society A: Mathematical,*
 918 *Physical and Engineering Sciences*, 468(2140), 913-931, doi:10.1098/rspa.2011.0422.
- 919 Bhatia, G. K., and S. Sahijpal (2017), Thermal evolution of trans-Neptunian objects, icy satellites,
 920 and minor icy planets in the early solar system, *Meteoritics & Planetary Science*, 52(12),
 921 2470-2490, doi:0.1111/maps.12952.
- 922 Bierson, C. J., F. Nimmo, and S. A. Stern (2020), Evidence for a hot start and early ocean formation
 923 on Pluto, *Nature Geoscience*, 13(7), 468-472, doi:10.1038/s41561-020-0595-0.
- 924 Billings, S. E., and S. A. Kattenhorn (2005), The great thickness debate: Ice shell thickness models
 925 for Europa and comparisons with estimates based on flexure at ridges, *Icarus*, 177(2), 397-
 926 412, doi:10.1016/j.icarus.2005.03.013.
- 927 Blankenship, D. D., D. A. Young, W. B. Moore, and J. C. Moore (2009), Radar sounding of
 928 Europa's subsurface properties and processes: The view from Earth, *Europa. University of*
 929 *Arizona Press, Tucson, AZ.*
- 930 Brown, E. K., et al. (2020), TRAPPED IN THE ICE: AN ANALYSIS OF BRINES IN BRITISH
 931 COLUMBIA'S HYPERSALINE LAKES, in *Lunar and Planetary Science Conference*,
 932 edited, Woodlands, TX.
- 933 Buffo, J. J. (2019), Multiphase reactive transport in planetary ices, Georgia Institute of
 934 Technology.
- 935 Buffo, J. J. (2020a), jbuffo/Liquidus-1.0: Liquidus-1.1 (Version v1.1), edited, Zenodo,
 936 doi:10.5281/zenodo.3774072.
- 937 Buffo, J. J. (2020b), jbuffo/SlushFund-2.0---Active-Interface-Tracking: SlushFund-2.0-Active-
 938 Interface-Tracking (Version v1.0), edited, Zenodo, doi:10.5281/zenodo.3774078.
- 939 Buffo, J. J., B. E. Schmidt, and C. Huber (2018), Multiphase Reactive Transport and Platelet Ice
 940 Accretion in the Sea Ice of McMurdo Sound, Antarctica, *Journal of Geophysical Research-*
 941 *Oceans*, 123(1), 324-345, doi:10.1002/2017jc013345.
- 942 Butler, B. M., S. Papadimitriou, A. Santoro, and H. Kennedy (2016), Mirabilite solubility in
 943 equilibrium sea ice brines, *Geochimica Et Cosmochimica Acta*, 182, 40-54,
 944 doi:10.1016/j.gca.2016.03.008.
- 945 Carr, M. H., et al. (1998), Evidence for a subsurface ocean on Europa, *Nature*, 391(6665), 363-
 946 365, doi:10.1038/34857.
- 947 Cassen, P., R. T. Reynolds, and S. Peale (1979), Is there liquid water on Europa?, *Geophysical*
 948 *Research Letters*, 6(9), 731-734, doi:10.1029/GL006i009p00731.
- 949 Charette, M. A., and W. H. Smith (2010), The volume of Earth's ocean, *Oceanography*, 23(2),
 950 112-114.
- 951 Chivers, C., J. Buffo, and B. Schmidt (2020), Thermal and Chemical Evolution of Small, Shallow
 952 Water Bodies on Europa, *LPI(2326)*, 1047.
- 953 Chivers, C. J., B. E. Schmidt, and J. J. Buffo (2019), Thermal and chemical evolution of shallow
 954 liquid water on Europa, paper presented at Outer Planets Assessment Group Meeting.

- 955 Chu, H., G. Chi, and I. M. Chou (2016), Freezing and melting behaviors of H₂O-NaCl-CaCl₂
956 solutions in fused silica capillaries and glass-sandwiched films: implications for fluid
957 inclusion studies, *Geofluids*, 16(3), 518-532, doi:10.1111/gfl.12173.
- 958 Chyba, C., and C. Phillips (2001), Possible ecosystems and the search for life on Europa, *Proc*
959 *Natl Acad Sci U S A*, 98(3), 801-804, doi:10.1073/pnas.98.3.801.
- 960 Collins, G., and F. Nimmo (2009), Chaotic terrain on Europa, in *Europa*, edited, pp. 259-281,
961 University of Arizona Press Tucson.
- 962 Cox, G., and W. Weeks (1988), Numerical simulations of the profile properties of undeformed
963 first-year sea ice during the growth season, *Journal of Geophysical Research: Oceans*,
964 93(C10), 12449-12460, doi:10.1029/JC093iC10p12449.
- 965 Craft, K. L., G. W. Patterson, R. P. Lowell, and L. Germanovich (2016), Fracturing and flow:
966 Investigations on the formation of shallow water sills on Europa, *Icarus*, 274, 297-313,
967 doi:10.1016/j.icarus.2016.01.023.
- 968 Craven, M., I. Allison, H. A. Fricker, and R. Warner (2009), Properties of a marine ice layer under
969 the Amery Ice Shelf, East Antarctica, *Journal of Glaciology*, 55(192), 717-728,
970 doi:10.3189/002214309789470941.
- 971 Davis, N. R., and P. Wadhams (1995), A Statistical-Analysis of Arctic Pressure Ridge
972 Morphology, *Journal of Geophysical Research-Oceans*, 100(C6), 10915-10925,
973 doi:10.1029/95jc00007.
- 974 Des Marais, D. J., et al. (2008), The NASA Astrobiology Roadmap, *Astrobiology*, 8(4), 715-730,
975 doi:10.1089/ast.2008.0819.
- 976 Dickson, A. G., and C. Goyet (1994), Handbook of methods for the analysis of the various
977 parameters of the carbon dioxide system in sea water. Version 2Rep., Oak Ridge National
978 Lab., TN (United States), doi:10.2172/10107773.
- 979 Doggett, T., R. Greeley, P. Figueredo, and K. Tanaka (2009), Geologic stratigraphy and evolution
980 of Europa's surface, in *Europa*, edited, pp. 137-160, University of Arizona Press Tucson,
981 AZ.
- 982 Durham, W., O. Prieto-Ballesteros, D. Goldsby, and J. Kargel (2010), Rheological and thermal
983 properties of icy materials, *Space Science Reviews*, 153(1-4), 273-298,
984 doi:10.1007/s11214-009-9619-1.
- 985 Durham, W. B., L. A. Stern, T. Kubo, and S. H. Kirby (2005), Flow strength of highly hydrated
986 Mg-and Na-sulfate hydrate salts, pure and in mixtures with water ice, with application to
987 Europa, *Journal of Geophysical Research: Planets*, 110(E12),
988 doi:10.1029/2005JE002475.
- 989 Eicken, H. (2003), From the microscopic, to the macroscopic, to the regional scale: growth,
990 microstructure and properties of sea ice, *Sea ice: an introduction to its physics, chemistry,*
991 *biology and geology*, 22-81.
- 992 Fagents, S. A. (2003), Considerations for effusive cryovolcanism on Europa: The post-Galileo
993 perspective, *Journal of Geophysical Research: Planets*, 108(E12),
994 doi:10.1029/2003JE002128.
- 995 Feltham, D. L., N. Untersteiner, J. S. Wettlaufer, and M. G. Worster (2006), Sea ice is a mushy
996 layer, *Geophysical Research Letters*, 33(14), doi:10.1029/2006gl026290.
- 997 Figueredo, P. H., and R. Greeley (2004), Resurfacing history of Europa from pole-to-pole
998 geological mapping, *Icarus*, 167(2), 287-312, doi:10.1016/j.icarus.2003.09.016.
- 999 Freitag, J. (1999). The hydraulic properties of Arctic sea ice-Implications for the small-scale
1000 particle transport. [in german] *Ber. Polarforsch*, 325, 150.

- 1001 Galton-Fenzi, B., J. Hunter, R. Coleman, S. Marsland, and R. Warner (2012), Modeling the basal
1002 melting and marine ice accretion of the Amery Ice Shelf, *Journal of Geophysical Research:
1003 Oceans*, 117(C9), doi:10.1029/2012JC008214.
- 1004 Golden, K. M., S. F. Ackley, and V. V. Lytle (1998), The percolation phase transition in sea ice,
1005 *Science*, 282(5397), 2238-2241, doi:10.1126/science.282.5397.2238.
- 1006 Golden, K. M., H. Eicken, A. L. Heaton, J. Miner, D. J. Pringle, and J. Zhu (2007), Thermal
1007 evolution of permeability and microstructure in sea ice, *Geophysical Research Letters*,
1008 34(16), doi:10.1029/2007gl030447.
- 1009 Greenberg, R., G. V. Hoppa, B. R. Tufts, P. Geissler, and J. Riley (1999), Chaos on Europa, *Icarus*,
1010 141(2), 263-286, doi:10.1006/icar.1999.6187.
- 1011 Griewank, P. J., and D. Notz (2013), Insights into brine dynamics and sea ice desalination from a
1012 1-D model study of gravity drainage, *Journal of Geophysical Research: Oceans*, 118(7),
1013 3370-3386, doi:10.1002/jgrc.20247.
- 1014 Gross, G. W., P. M. Wong, and K. Humes (1977), Concentration dependent solute redistribution
1015 at the ice–water phase boundary. III. Spontaneous convection. Chloride solutions, *The
1016 Journal of chemical physics*, 67(11), 5264-5274, doi:10.1063/1.434704.
- 1017 Han, L., and A. P. Showman (2005), Thermo-compositional convection in Europa's icy shell with
1018 salinity, *Geophysical research letters*, 32(20), doi:10.1029/2005GL023979.
- 1019 Hand, K. P., and C. F. Chyba (2007), Empirical constraints on the salinity of the european ocean
1020 and implications for a thin ice shell, *Icarus*, 189(2), 424-438,
1021 doi:10.1016/j.icarus.2007.02.002.
- 1022 Hendrix, A. R., et al. (2019), The NASA Roadmap to Ocean Worlds, *Astrobiology*, 19(1), 1-27,
1023 doi:10.1089/ast.2018.1955.
- 1024 Howell, S. M., and R. T. Pappalardo (2018), Band formation and ocean-surface interaction on
1025 Europa and Ganymede, *Geophysical Research Letters*, 45(10), 4701-4709,
1026 doi:10.1029/2018GL077594.
- 1027 Howell, S. M., and R. T. Pappalardo (2019), Can Earth-like plate tectonics occur in ocean world
1028 ice shells?, *Icarus*, 322, 69-79, doi:10.1016/j.icarus.2019.01.011.
- 1029 Huber, C., A. Parmigiani, B. Chopard, M. Manga, and O. Bachmann (2008), Lattice Boltzmann
1030 model for melting with natural convection, *International Journal of Heat and Fluid Flow*,
1031 29(5), 1469-1480, doi:10.1016/j.ijheatfluidflow.2008.05.002.
- 1032 Hunke, E. C., D. Notz, A. K. Turner, and M. Vancoppenolle (2011), The multiphase physics of
1033 sea ice: a review for model developers, *Cryosphere*, 5(4), 989-1009, doi:10.5194/tc-5-989-
1034 2011.
- 1035 Huppert, H. E., and M. G. Worster (1985), Dynamic Solidification of a Binary Melt, *Nature*,
1036 314(6013), 703-707, doi:10.1038/314703a0.
- 1037 Hussmann, H., T. Spohn, and K. Wiczerkowski (2002), Thermal equilibrium states of Europa's
1038 ice shell: Implications for internal ocean thickness and surface heat flow, *Icarus*, 156(1),
1039 143-151, doi:10.1006/icar.2001.6776.
- 1040 Intergovernmental Oceanographic Commission; Scientific Committee on Oceanic Research;
1041 International Association for the Physical Sciences of the Oceans (2015), The International
1042 thermodynamic equation of seawater – 2010: calculation and use of thermodynamic
1043 properties. [includes corrections up to 31st October 2015] . Paris, France, UNESCO,
1044 196pp. (Intergovernmental Oceanographic Commission Manuals and
1045 Guides;56). <http://hdl.handle.net/11329/286>

- 1046 Johnson, B. C., R. Y. Sheppard, A. C. Pascuzzo, E. A. Fisher, and S. E. Wiggins (2017a), Porosity
1047 and Salt Content Determine if Subduction Can Occur in Europa's Ice Shell, *Journal of*
1048 *Geophysical Research: Planets*, 122(12), 2765-2778, doi:10.1002/2017je005370.
- 1049 Johnson, B. C., R. Y. Sheppard, A. C. Pascuzzo, E. A. Fisher, and S. E. Wiggins (2017b), Porosity
1050 and Salt Content Determine if Subduction Can Occur in Europa's Ice Shell, *Journal of*
1051 *Geophysical Research-Planets*, 122(12), 2765-2778, doi:10.1002/2017je005370.
- 1052 Journaux, B., J. M. Brown, A. Pakhomova, I. E. Collings, S. Petitgirard, P. Espinoza, T. Boffa
1053 Ballaran, S. D. Vance, J. Ott, and F. Cova (2020), Holistic Approach for Studying Planetary
1054 Hydrospheres: Gibbs Representation of Ices Thermodynamics, Elasticity, and the Water
1055 Phase Diagram to 2,300 MPa, *Journal of Geophysical Research: Planets*, 125(1),
1056 doi:10.1029/2019JE006176.
- 1057 Kalousova, K., D. M. Schroeder, and K. M. Soderlund (2017), Radar attenuation in Europa's ice
1058 shell: Obstacles and opportunities for constraining the shell thickness and its thermal
1059 structure, *Journal of Geophysical Research-Planets*, 122(3), 524-545,
1060 doi:10.1002/2016je005110.
- 1061 Kalousová, K., O. Souček, G. Tobie, G. Choblet, and O. Čadek (2014), Ice melting and downward
1062 transport of meltwater by two-phase flow in Europa's ice shell, *Journal of Geophysical*
1063 *Research: Planets*, 119(3), 532-549, doi:10.1002/2013JE004563.
- 1064 Kalousová, K., O. Souček, G. Tobie, G. Choblet, and O. Čadek (2016), Water generation and
1065 transport below Europa's strike-slip faults, *Journal of Geophysical Research: Planets*,
1066 121(12), 2444-2462, doi:10.1002/2016JE005188.
- 1067 Kargel, J. S., J. Z. Kaye, J. W. Head, G. M. Marion, R. Sassen, J. K. Crowley, O. Prieto Ballesteros,
1068 S. A. Grant, and D. L. Hogenboom (2000), Europa's crust and ocean: Origin, composition,
1069 and the prospects for life, *Icarus*, 148(1), 226-265, doi:10.1006/icar.2000.6471.
- 1070 Kattenhorn, S. A. (2018), Commentary: The Feasibility of Subduction and Implications for Plate
1071 Tectonics on Jupiter's moon Europa, doi:10.1002/2018JE005524.
- 1072 Kattenhorn, S. A., and L. M. Prockter (2014), Evidence for subduction in the ice shell of Europa,
1073 *Nature Geoscience*, 7(10), 762-767, doi:10.1038/Ngeo2245.
- 1074 Khazendar, A., E. Rignot, and E. Larour (2009), Roles of marine ice, rheology, and fracture in the
1075 flow and stability of the Brunt/Stancomb-Wills Ice Shelf, *Journal of Geophysical*
1076 *Research: Earth Surface*, 114(F4), doi:10.1029/2008JF001124.
- 1077 Khurana, K. K., M. G. Kivelson, D. J. Stevenson, G. Schubert, C. T. Russell, R. J. Walker, and C.
1078 Polanskey (1998), Induced magnetic fields as evidence for subsurface oceans in Europa
1079 and Callisto, *Nature*, 395(6704), 777-780, doi:10.1038/27394.
- 1080 Kivelson, M. G., K. K. Khurana, C. T. Russell, M. Volwerk, R. J. Walker, and C. Zimmer (2000),
1081 Galileo magnetometer measurements: A stronger case for a subsurface ocean at Europa,
1082 *Science*, 289(5483), 1340-1343, doi:10.1126/science.289.5483.1340.
- 1083 Kurtz, N. T., and T. Markus (2012), Satellite observations of Antarctic sea ice thickness and
1084 volume, *Journal of Geophysical Research-Oceans*, 117(C8), doi:10.1029/2012jc008141.
- 1085 Laxon, S. W., K. A. Giles, A. L. Ridout, D. J. Wingham, R. Willatt, R. Cullen, R. Kwok, A.
1086 Schweiger, J. Zhang, and C. Haas (2013), CryoSat-2 estimates of Arctic sea ice thickness
1087 and volume, *Geophysical Research Letters*, 40(4), 732-737, doi:10.1002/grl.50193.
- 1088 Leonard, E. J., R. T. Pappalardo, and A. Yin (2018), Analysis of very-high-resolution Galileo
1089 images and implications for resurfacing mechanisms on Europa, *Icarus*, 312, 100-120,
1090 doi:10.1016/j.icarus.2018.04.016.

- 1091 Lyon, W. (1961), DIVISION OF OCEANOGRAPHY AND METEOROLOGY: OCEAN AND
1092 SEA-ICE RESEARCH IN THE ARCTIC OCEAN VIA SUBMARINE, *Transactions of*
1093 *the New York Academy of Sciences*, 23(8 Series II), 662-674, doi:10.1111/j.2164-
1094 0947.1961.tb01400.x.
- 1095 Malmgren, F. (1927), *On the properties of sea-ice*, AS John Griegs Boktrykkeri.
- 1096 Manga, M., and C. Michaut (2017), Formation of lenticulae on Europa by saucer-shaped sills,
1097 *Icarus*, 286, 261-269, doi:10.1016/j.icarus.2016.10.009.
- 1098 Manga, M., and C. Y. Wang (2007), Pressurized oceans and the eruption of liquid water on Europa
1099 and Enceladus, *Geophysical Research Letters*, 34(7), doi:10.1029/2007gl029297.
- 1100 Marion, G. M., J. S. Kargel, D. C. Catling, and S. D. Jakubowski (2005), Effects of pressure on
1101 aqueous chemical equilibria at subzero temperatures with applications to Europa,
1102 *Geochimica Et Cosmochimica Acta*, 69(2), 259-274, doi:10.1016/j.gca.2004.06.024.
- 1103 McCarthy, C., J. R. Blackford, and C. E. Jeffree (2013), Low-temperature-SEM study of dihedral
1104 angles in the ice-I/sulfuric acid partially molten system, *J Microsc*, 249(2), 150-157,
1105 doi:10.1111/jmi.12003.
- 1106 McCarthy, C., R. F. Cooper, D. L. Goldsby, W. B. Durham, and S. H. Kirby (2011), Transient and
1107 steady state creep response of ice I and magnesium sulfate hydrate eutectic aggregates,
1108 *Journal of Geophysical Research-Planets*, 116(E4), doi:10.1029/2010je003689.
- 1109 McCarthy, C., R. F. Cooper, S. H. Kirby, K. D. Rieck, and L. A. Stern (2007), Solidification and
1110 microstructures of binary ice-I/hydrate eutectic aggregates, *American Mineralogist*,
1111 92(10), 1550-1560, doi:10.2138/am.2007.2435.
- 1112 McCarthy, C., M. A. Nielson, A. N. Coonin, J. S. Minker, and A. A. Domingos (2019), Acoustic
1113 and Microstructural Properties of Partially Molten Samples in the Ice-Ammonia System,
1114 *Geosciences*, 9(8), 327, doi:10.3390/geosciences9080327.
- 1115 McCord, T. B., G. B. Hansen, D. L. Matson, T. V. Johnson, J. K. Crowley, F. P. Fanale, R. W.
1116 Carlson, W. D. Smythe, P. D. Martin, and C. A. Hibbitts (1999), Hydrated salt minerals on
1117 Europa's surface from the Galileo near-infrared mapping spectrometer (NIMS)
1118 investigation, *Journal of Geophysical Research: Planets*, 104(E5), 11827-11851,
1119 doi:10.1029/1999JE900005.
- 1120 McCord, T. B., G. Teeter, G. B. Hansen, M. T. Sieger, and T. M. Orlando (2002), Brines exposed
1121 to Europa surface conditions, *Journal of Geophysical Research-Planets*, 107(E1), 4-1-4-6,
1122 doi:10.1029/2000je001453.
- 1123 McDougall, T. J., and P. M. Barker (2011), Getting started with TEOS-10 and the Gibbs Seawater
1124 (GSW) oceanographic toolbox, *SCOR/IAPSO WG*, 127, 1-28.
- 1125 McKinnon, W. B. (1999), Convective instability in Europa's floating ice shell, *Geophysical*
1126 *Research Letters*, 26(7), 951-954, doi:10.1029/1999gl900125.
- 1127 McKinnon, W. B., and M. E. Zolensky (2003), Sulfate content of Europa's ocean and shell:
1128 Evolutionary considerations and some geological and astrobiological implications,
1129 *Astrobiology*, 3(4), 879-897, doi:10.1089/153110703322736150.
- 1130 Michaut, C., and M. Manga (2014), Domes, pits, and small chaos on Europa produced by water
1131 sills, *Journal of Geophysical Research: Planets*, 119(3), 550-573,
1132 doi:10.1002/2013JE004558.
- 1133 Mitri, G., and A. P. Showman (2005), Convective-conductive transitions and sensitivity of a
1134 convecting ice shell to perturbations in heat flux and tidal-heating rate: Implications for
1135 Europa, *Icarus*, 177(2), 447-460, doi:10.1016/j.icarus.2005.03.019.

- 1136 Nakawo, M., and N. K. Sinha (1981), Growth rate and salinity profile of first-year sea ice in the
1137 high Arctic, *Journal of Glaciology*, 27(96), 315-330, doi:10.3189/S0022143000015409.
- 1138 Nakawo, M., and N. K. Sinha (1984), A note on brine layer spacing of first-year sea ice,
1139 *Atmosphere-ocean*, 22(2), 193-206, doi:10.1080/07055900.1984.9649193.
- 1140 National Research Council (2012), Assessment of Planetary Protection Requirements for
1141 Spacecraft Missions to Icy Solar System Bodies. Washington, DC: The National
1142 Academies Press. <https://doi.org/10.17226/13401>.
- 1143 National Research Council (2011), Vision and Voyages for Planetary Science in the Decade 2013-
1144 2022. Washington, DC: The National Academies Press. <https://doi.org/10.17226/13117>.
- 1145 Neveu, M., S. J. Desch, and J. C. Castillo-Rogez (2017), Aqueous geochemistry in icy world
1146 interiors: Equilibrium fluid, rock, and gas compositions, and fate of antifreezes and
1147 radionuclides, *Geochimica Et Cosmochimica Acta*, 212, 324-371,
1148 doi:10.1016/j.gca.2017.06.023.
- 1149 Nimmo, F., and E. Gaidos (2002), Strike-slip motion and double ridge formation on Europa,
1150 *Journal of Geophysical Research: Planets*, 107(E4), 5-1-5-8, doi:10.1029/2000JE001476.
- 1151 Nimmo, F., B. Giese, and R. Pappalardo (2003), Estimates of Europa's ice shell thickness from
1152 elastically-supported topography, *Geophysical Research Letters*, 30(5),
1153 doi:10.1029/2002GL016660.
- 1154 Notz, D., and M. G. Worster (2009), Desalination processes of sea ice revisited, *Journal of*
1155 *Geophysical Research-Oceans*, 114(C5), doi:10.1029/2008jc004885.
- 1156 Oren, A. (2013), Life in magnesium-and calcium-rich hypersaline environments: salt stress by
1157 chaotropic ions, in *Polyextremophiles*, edited, pp. 215-232, Springer, doi: 10.1007/978-
1158 94-007-6488-0_8.
- 1159 Pappalardo, R., M. Belton, H. Breneman, M. Carr, C. Chapman, G. Collins, T. Denk, S. Fagents,
1160 P. Geissler, and B. Giese (1999), Does Europa have a subsurface ocean? Evaluation of the
1161 geological evidence, *Journal of Geophysical Research: Planets*, 104(E10), 24015-24055,
1162 doi:10.1029/1998JE000628.
- 1163 Pappalardo, R., D. Senske, H. Korth, R. Klima, S. Vance, and K. Craft (2017), The Europa Clipper
1164 Mission: Exploring The Habitability of A Unique Icy World, paper presented at European
1165 Planetary Science Congress.
- 1166 Pappalardo, R. T., and A. C. Barr (2004), The origin of domes on Europa: The role of thermally
1167 induced compositional diapirism, *Geophysical Research Letters*, 31(1),
1168 doi:10.1029/2003gl019202.
- 1169 Phillips, C. B., and R. T. Pappalardo (2014), Europa Clipper mission concept: Exploring Jupiter's
1170 ocean moon, *Eos, Transactions American Geophysical Union*, 95(20), 165-167,
1171 doi:10.1002/2014EO200002.
- 1172 Plaut, J. (2019). RIME and REASON on JUICE and Clipper: A comprehensive campaign to probe
1173 the icy satellites of Jupiter. *EPSC, 2019*, EPSC-DPS2019.
- 1174 Pontefract, A., C. E. Carr, and M. R. Osburn (2019), The Role of Ionic Composition and
1175 Concentration on Biosignature Preservation: Lessons from the “Spotted” Lakes of British
1176 Colombia, paper presented at 2019 Astrobiology Science Conference, AGU.
- 1177 Pontefract, A., T. F. Zhu, V. K. Walker, H. Hepburn, C. Lui, M. T. Zuber, G. Ruvkun, and C. E.
1178 Carr (2017), Microbial Diversity in a Hypersaline Sulfate Lake: A Terrestrial Analog of
1179 Ancient Mars, *Front Microbiol*, 8, 1819, doi:10.3389/fmicb.2017.01819.

- 1180 Renaut, R. W., and P. R. Long (1989), Sedimentology of the Saline Lakes of the Cariboo Plateau,
1181 Interior British-Columbia, Canada, *Sedimentary Geology*, 64(4), 239-264,
1182 doi:10.1016/0037-0738(89)90051-1.
- 1183 Reynolds, R. T., S. W. Squyres, D. S. Colburn, and C. P. McKay (1983), On the Habitability of
1184 Europa, *Icarus*, 56(2), 246-254, doi:10.1016/0019-1035(83)90037-4.
- 1185 Rolle, M., and T. Le Borgne (2019), Mixing and Reactive Fronts in the Subsurface, *Reactive*
1186 *Transport in Natural and Engineered Systems*, 85(1), 111-142,
1187 doi:10.2138/rmg.2018.85.5.
- 1188 Ross, M., and G. Schubert (1987), Tidal heating in an internal ocean model of Europa, *Nature*,
1189 325(6100), 133-134.
- 1190 Rubištejn, L. (2000), *The stefan problem*, American Mathematical Soc.
- 1191 Russell, M. J., A. E. Murray, and K. P. Hand (2017), The Possible Emergence of Life and
1192 Differentiation of a Shallow Biosphere on Irradiated Icy Worlds: The Example of Europa,
1193 *Astrobiology*, 17(12), 1265-1273, doi:10.1089/ast.2016.1600.
- 1194 Schmidt, B. (2020), The Astrobiology of Europa and the Jovian System, *Planetary Astrobiology*,
1195 185, doi:10.2458/azu_uapress_9780816540068-ch008.
- 1196 Schmidt, B. E., D. D. Blankenship, G. W. Patterson, and P. M. Schenk (2011), Active formation
1197 of 'chaos terrain' over shallow subsurface water on Europa, *Nature*, 479(7374), 502-505,
1198 doi:10.1038/nature10608.
- 1199 Schroeder, D. M., A. Romero-Wolf, L. Carrer, C. Grima, B. A. Campbell, W. Kofman, L.
1200 Bruzzone, and D. D. Blankenship (2016), Assessing the potential for passive radio
1201 sounding of Europa and Ganymede with RIME and REASON, *Planetary and Space*
1202 *Science*, 134, 52-60, doi:10.1016/j.pss.2016.10.007.
- 1203 Soderlund, K. M., B. E. Schmidt, J. Wicht, and D. D. Blankenship (2014), Ocean-driven heating
1204 of Europa's icy shell at low latitudes, *Nature Geoscience*, 7(1), 16-19,
1205 doi:10.1038/Ngeo2021.
- 1206 Sparks, W. B., B. E. Schmidt, M. A. McGrath, K. P. Hand, J. Spencer, M. Cracraft, and S. E.
1207 Deustua (2017), Active cryovolcanism on Europa?, *The Astrophysical Journal Letters*,
1208 839(2), L18.
- 1209 Squyres, S. W., R. T. Reynolds, P. M. Cassen, and S. J. Peale (1983), Liquid Water and Active
1210 Resurfacing on Europa, *Nature*, 301(5897), 225-226, doi:10.1038/301225a0.
- 1211 Thomas, E. C., R. Hodyss, T. H. Vu, P. V. Johnson, and M. Choukroun (2017), Composition and
1212 Evolution of Frozen Chloride Brines under the Surface Conditions of Europa, *Acs Earth*
1213 *and Space Chemistry*, 1(1), 14-23, doi:10.1021/acsearthspacechem.6b00003.
- 1214 Tobie, G., G. Choblet, and C. Sotin (2003), Tidally heated convection: Constraints on Europa's ice
1215 shell thickness, *Journal of Geophysical Research: Planets*, 108(E11),
1216 doi:10.1029/2003JE002099.
- 1217 Toner, J. D., D. C. Catling, and B. Light (2014), The formation of supercooled brines, viscous
1218 liquids, and low-temperature perchlorate glasses in aqueous solutions relevant to Mars,
1219 *Icarus*, 233, 36-47, doi:10.1016/j.icarus.2014.01.018.
- 1220 Turner, A. K., and E. C. Hunke (2015), Impacts of a mushy-layer thermodynamic approach in
1221 global sea-ice simulations using the CICE sea-ice model, *Journal of Geophysical*
1222 *Research: Oceans*, 120(2), 1253-1275, doi:10.1002/2014JC010358.
- 1223 Turner, A. K., E. C. Hunke, and C. M. Bitz (2013), Two modes of sea-ice gravity drainage: A
1224 parameterization for large-scale modeling, *Journal of Geophysical Research: Oceans*,
1225 118(5), 2279-2294, doi:10.1002/jgrc.20171.

- 1226 Untersteiner, N. (1968), Natural Desalination and Equilibrium Salinity Profile of Perennial Sea
1227 Ice, *Journal of Geophysical Research*, 73(4), 1251-+, doi:10.1029/JB073i004p01251.
- 1228 Vance, S. D., L. M. Barge, S. S. S. Cardoso, and J. H. E. Cartwright (2019), Self-Assembling Ice
1229 Membranes on Europa: Brinicle Properties, Field Examples, and Possible Energetic
1230 Systems in Icy Ocean Worlds, *Astrobiology*, 19(5), 685-695, doi:10.1089/ast.2018.1826.
- 1231 Vance, S. D., K. P. Hand, and R. T. Pappalardo (2016), Geophysical controls of chemical
1232 disequilibria in Europa, *Geophysical Research Letters*, 43(10), 4871-4879,
1233 doi:10.1002/2016gl068547.
- 1234 Vilella, K., G. Choblet, W. E. Tsao, and F. Deschamps (2020), Tidally Heated Convection and the
1235 Occurrence of Melting in Icy Satellites: Application to Europa, *Journal of Geophysical
1236 Research-Planets*, 125(3), e2019JE006248, doi:10.1029/2019JE006248.
- 1237 Walker, C., and B. Schmidt (2015), Ice collapse over trapped water bodies on Enceladus and
1238 Europa, *Geophysical Research Letters*, 42(3), 712-719, doi:10.1002/2014GL062405.
- 1239 Walker, C., B. Schmidt, and J. Bassis (2014), Breaking the ice: On the application of fracture
1240 system mechanics and fragmentation theory to the chaos regions of Europa, *LPI(1777)*,
1241 2659.
- 1242 Weeks, W., and G. Lofgren (1967), The effective solute distribution coefficient during the freezing
1243 of NaCl solutions, *Physics of Snow and Ice: proceedings*, 1(1), 579-597.
- 1244 Weeks, W. F., and S. F. Ackley (1986), The growth, structure, and properties of sea ice, in *The
1245 geophysics of sea ice*, edited, pp. 9-164, Springer.
- 1246 Weller, M. B., L. Fuchs, T. W. Becker, and K. M. Soderlund (2019), Convection in Thin Shells of
1247 Icy Satellites: Effects of Latitudinal Surface Temperature Variations, *Journal of
1248 Geophysical Research-Planets*, 124(8), 2029-2053, doi:10.1029/2018je005799.
- 1249 Wells, A. J., J. S. Wettlaufer, and S. A. Orszag (2011), Brine fluxes from growing sea ice,
1250 *Geophysical Research Letters*, 38(4), doi:10.1029/2010gl046288.
- 1251 Worster, M. G. (1991), Natural-Convection in a Mushy Layer, *Journal of Fluid Mechanics*, 224,
1252 335-359, doi:10.1017/S0022112091001787.
- 1253 Worster, M. G., and D. W. Rees Jones (2015), Sea-ice thermodynamics and brine drainage, *Philos
1254 Trans A Math Phys Eng Sci*, 373(2045), 20140166, doi:10.1098/rsta.2014.0166.
- 1255 Zolotov, M. Y., and J. Kargel (2009), *On the chemical composition of Europa's icy shell, ocean,
1256 and underlying rocks*, University of Arizona Press Tucson, AZ.
- 1257 Zolotov, M. Y., E. Shock, A. Barr, and R. Pappalardo (2004), Brine pockets in the icy shell on
1258 Europa: Distribution, chemistry, and habitability.
- 1259 Zolotov, M. Y., and E. L. Shock (2001), Composition and stability of salts on the surface of Europa
1260 and their oceanic origin, *Journal of Geophysical Research-Planets*, 106(E12), 32815-
1261 32827, doi:10.1029/2000je001413.
- 1262 Zotikov, I. A., V. S. Zagorodnov, and J. V. Raikovsky (1980), Core Drilling through the Ross Ice
1263 Shelf (Antarctica) Confirmed Basal Freezing, *Science*, 207(4438), 1463-1464,
1264 doi:10.1126/science.207.4438.1463.
- 1265